JPEDAV (2015) 36:149–168
DOI: 10.1007/s11669-015-0368-4
1547-7037 ©ASM International

Liquidus Projection Surface and Isothermal Section at 1200 °C of Ni-Ru-Y

S.H. Coetzee, L.A. Cornish, M.J. Witcomb, and P.K. Jain

(Submitted June 18, 2014; in revised form January 9, 2015; published online February 18, 2015)

Scanning electron microscopy studies with energy dispersive x-ray analyses of as-cast and annealed samples of Ni-Ru-Y were used to produce a solidification projection, a liquidus projection surface and an isothermal section at 1200 °C. The ∼YNi_2, ∼YNi_3 and ∼YRu_2 phases had wider solubilities than line compounds, and also extended the furthest into the system. The binary phase extensions into the ternary were: ∼51 at.% Ru for ∼YNi_2; ∼22 at.% Ru for ∼YNi_3; ∼13 at.% Ru for ∼YNi_5; ∼7 at.% Ru for ∼YNi; ∼12 at.% Ni for ∼YRu_2 and ∼10 at.% for ∼$Y_{44}Ru_{25}$. Ruthenium stabilised ∼YNi_2, so that it solidified at a higher temperature in the ternary than in the Ni-Y binary. A ternary phase was confirmed at $Y_{51}Ru_{15}Ni_{34}$ (at.%), which forms in a peritectic reaction. The ∼Y_3Ru and ∼Y_3Ni phases were isomorphous and formed a continuous solid solution. Heat treatment at 1200 °C gave the phases: (Ru), ∼YRu_2, ∼YNi_2, ∼YNi_3, ∼YNi_4, ∼YNi_5 and (Y).

Keywords scanning electron microscopy (SEM), energy dispersive spectrometry (EDS), isothermal section 1200 °C, liquidus surface projection, Ni-Ru-Y, ternary phase diagram

1. Introduction

The Ni-Ru-Y system was studied for a potential new coating material. It is of interest because ruthenium increases the corrosion resistance of titanium alloys,[1] hardmetals[2] and stainless steels,[3] and yttrium has been used as a component for coating Ni-based alloys.[4]

The Ni-Ru (Fig. 1) and Ni-Y (Fig. 2) binary phase diagrams are well established, but the reactions in Ru-Y are less certain, although the phases are known (Fig. 3).[5] The Ni-Y and Ru-Y phase diagrams are complex with many phases,[5] whereas Ni-Ru is a simple peritectic, with no intermetallic phases.

A structure type for $Y(Ru_xNi_{1-x})_2$, where $x = 0 - 0.78$ (i.e. ∼YNi_2 up to $Y_{33}Ru_{52}Ni_{15}$) was reported as Cu_2Mg.[6] Chunxiao et al.[7] studied the transect from YNi_2 to YRu_2 in Ni-Ru-Y and found a two-phase region between the binary phase extensions, and that ∼YNi_2 extended much further into the ternary than ∼YRu_2. Both YNi_2 and YRu_2 are Laves phases; YNi_2 has the Cu_2Mg structure, and YRu_2 has the Zn_2Mg structure.[8]

Sokolovskaya et al.[9] produced an isothermal section at 600 °C for Ni-Ru-Y. For the terminal solid solutions, (Ni) was shown with solubility for only ruthenium, and (Ru) was shown with considerable solubility for nickel. In the redrawn version (Fig. 4),[10,11] (Ru) was drawn with less solubility for Ni, but both solubilities decrease with temperature,[5] and phases which had previously been drawn as line compounds,[9] were drawn with small solubility ranges. Not all of the accepted binary intermetallic phases[5] were indicated on the isothermal section, and the missing phases were: Y_2Ni_7, Y_3Ni_2, Y_3Ru_2, $Y_{44}Ru_{25}$ and Y_5Ru_2. The reason for this is probably that the phases did not penetrate the ternary sufficiently for the samples to contain them, and the original paper[9] did not provide sample compositions. There was no solubility shown in Y. All the binary phases present were shown to extend into the ternary as line compounds, along constant Y content.[9] At 600 °C, the extent of ∼Y_3Ni was at ∼Y_{75}:Ru_6:Ni_{19} (at.%) and the extent of ∼Y_3Ru was at Y_{75}:Ru_{17}:Ni_8 (at.%). The phase extents of ∼YNi_2 and ∼YRu_2 agreed well with Chugxiao et al.[7] and these phases extended towards each other, with a two-phase region between. It should be noted that, considering the tie-triangles (three-phase regions) and the two-phase regions, there are no true ternary phases on that transect, and the extents of the YNi_2 and YRu_2 phases are ∼Y_{34}:Ru_{49}:Ni_{17} and ∼Y_{34}:Ru_{55}:Ni_{11} (at.%) respectively. These phase extension limits are marked on the most

S.H. Coetzee, Electron Microscope Unit, University of Botswana, Private Bag 0022, Gaborone, Botswana and African Materials and Engineering Network (AMSEN, a Carnegie-IAS RISE Network), Wits, Braamfontein, South Africa; L.A. Cornish, African Materials and Engineering Network (AMSEN, a Carnegie-IAS RISE Network), Wits, Braamfontein, South Africa, DST-NRF Centre of Excellence in Strong Materials, University of the Witwatersrand, Private Bag 3, WITS, 2050, Johannesburg, South Africa, and School of Chemical and Metallurgical Engineering, University of the Witwatersrand, Private Bag 3, WITS, 2050, Johannesburg, South Africa; **M.J. Witcomb**, African Materials and Engineering Network (AMSEN, a Carnegie-IAS RISE Network), Wits, Braamfontein, South Africa and DST-NRF Centre of Excellence in Strong Materials, University of the Witwatersrand, Private Bag 3, WITS, 2050, Johannesburg, South Africa; and **P.K. Jain**, African Materials and Engineering Network (AMSEN, a Carnegie-IAS RISE Network), Wits, Braamfontein, South Africa and Department of Physics, University of Botswana, Private Bag 0022, Gaborone, Botswana.Contact e-mail: coetzeesh@yahoo.co.uk

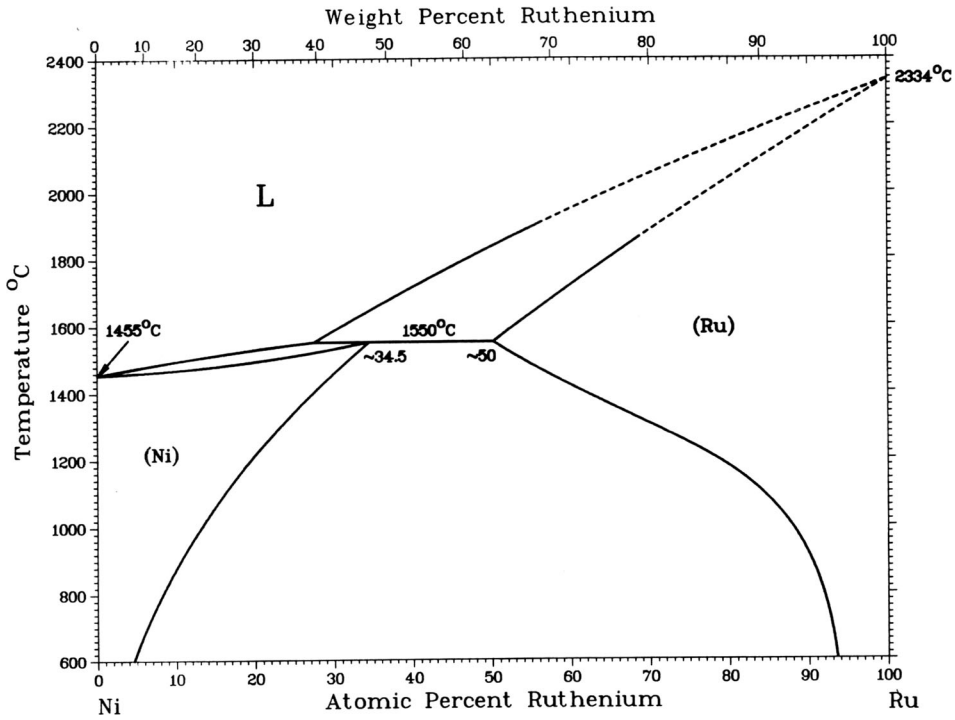

Fig. 1 Ni-Ru phase diagram[5]

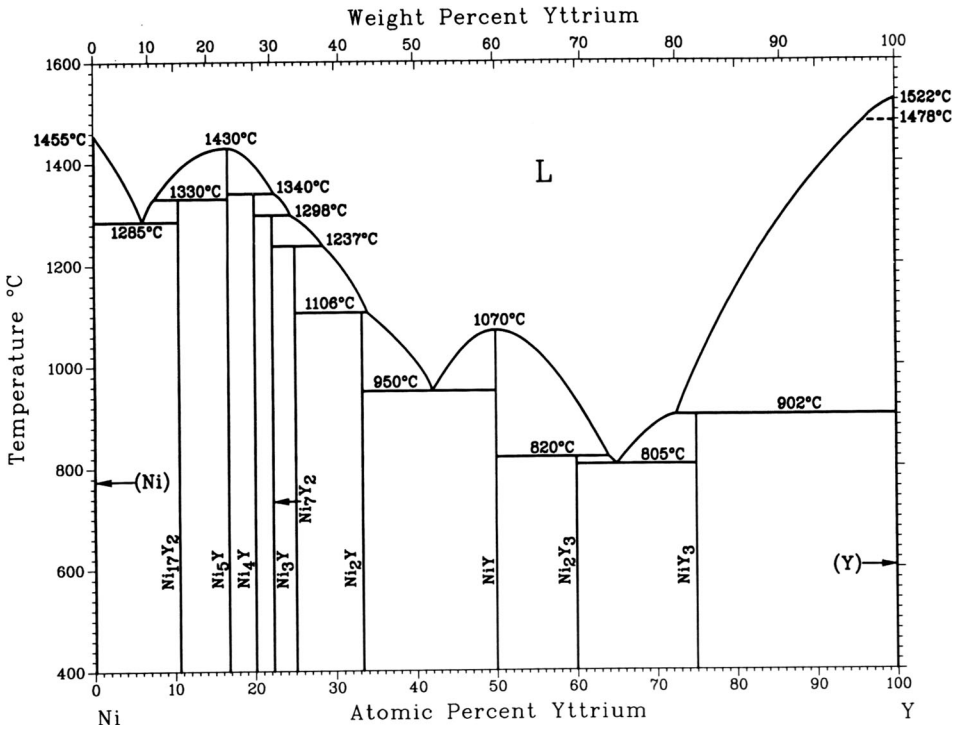

Fig. 2 Ni-Y phase diagram[5]

recent compilation diagrams.[10,11] The phase widths were drawn to be ~1 at.% in the compilation (Fig. 4),[11,12] wider than in the original.[9] A true ternary phase, $\sim Y_5Ru_2Ni_2$,[9] was reported with a solubility range of ~5 at.%, which was involved in four three-phase fields,[9] but in the subsequent compilations,[10,11] the range was smaller. In this investigation, the ternary phase is denoted τ, or $\sim Y_{51}Ru_{15}Ni_{34}$ (at.%).

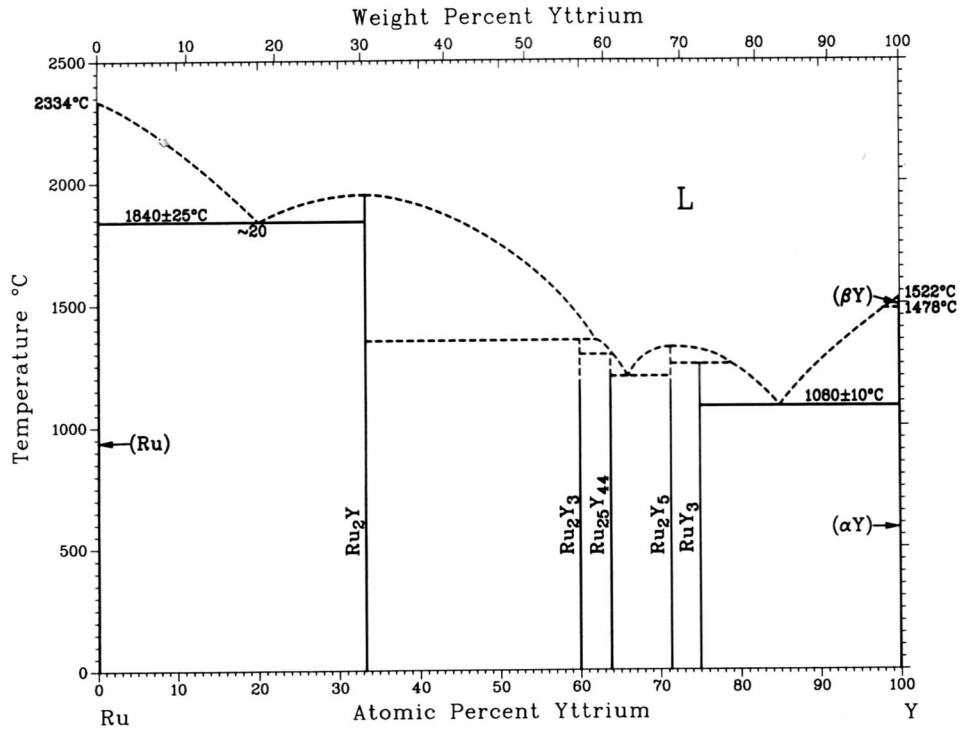

Fig. 3 Ru-Y phase diagram[5]

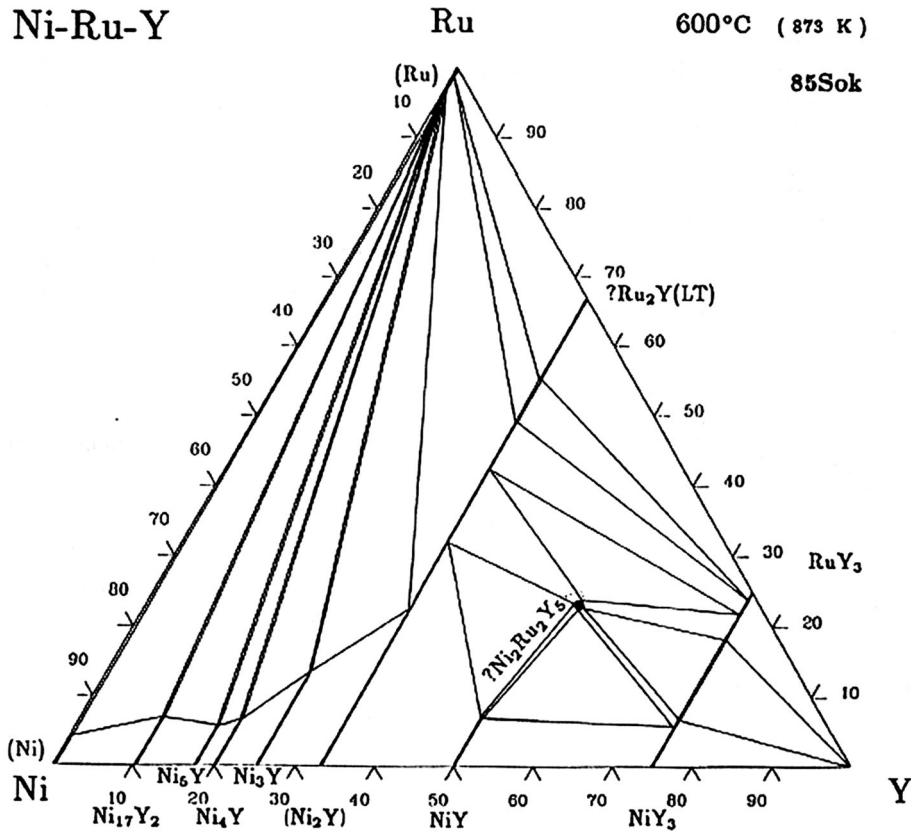

Fig. 4 Isothermal section of Ni-Ru-Y (at.%) at 600 °C[10,11], redrawn from Sokolovskaya et al[9]

Table 1 Starting elements

Element	Purity	Condition	Impurities, ppm	Supplier
Ni	99.99+%	Powder 150 μm max	Ag 1, Al 1, Ca 1, Cr < 1, Cu 3, Fe 15, Mg < 1, Mn < 1, Si 2, Sn < 1	1
Ru	99.9%	Lump	Unknown	2
Y	99.9%	Lump	Al 10, Ca 30, Cu 10, Dy 2, Er 2, Eu 12, Fe 15, Gd 30, Mg 5, Si 10, Ta 300, Tm 1, Yb 5	1

1 Purchased from Goodfellow Cambridge Ltd., Huntingdon, England
2 From the Platinum Development Initiative (PDI) (Anglo Platinum, Lonmin and Impala) through Mintek, South Africa

The aim of this work was to study as-cast alloys, and derive a liquidus surface. Additionally, samples were annealed at 1200 °C, and compared to the lower temperature results of the isothermal section at 600 °C.[9,10] The phase nomenclature is given in Pettifor order.[12] Although some preliminary work has already been published from the current study,[13-19] this is the final version, and some of the interpretations have been changed using evidence from more samples.

2. Experimental Procedure

The samples were made by arc-melting minimum 99.9% pure elemental components, Table 1, under an argon atmosphere, after pumping out and flushing repeatedly with argon, and titanium was used as an oxygen-getter. The samples were then sectioned, as near as possible into halves, mounted, and prepared metallographically. The first five samples were also sealed in silica ampoules, back-filled with argon, and annealed at 1200 °C (rather than the planned 1000 °C) for 1000 h. Although there was a concern that Y could reduce SiO_2, there were no other methods available.

Analyses were undertaken using pure element standards, in a Philips XL 30 ESEM with an EDAX Phoenix EDX system, and at least five analyses were taken on different phases or over areas to obtain the averages presented. The phases were identified by comparing the compositions to the 600 °C isothermal section,[9] the binaries[5] and also using the phase morphologies in the microstructures. When not in use, the samples were stored in ethanol or methanol. Unfortunately, most of the samples oxidized and disintegrated before x-ray diffraction (XRD) could be undertaken to confirm the phases, but some were analysed on a Philips PW 3710 powder diffractometer giving patterns of poor quality.

3. Results

Some of the alloys had small particles of Y_2O_3, which were assumed to be present before, or in an early stage of melting, despite taking the precautions of melting under argon and storing in alcohol. Since the oxide particles were mainly in minor proportions, and have a very high melting point (2458 °C),[5] they were ignored in the interpretation of the microstructures, despite the fact that they were sometimes nucleation sites. Although these particles were analysed, being more brittle, they were usually at least partially removed on sample preparation and the resulting poor surface gave low wt% totals and high errors. Ignoring the oxides in the samples' compositions, the solidification sequences were justified since attempts to interpret them as (Y), which then subsequently oxidized, gave impossible solidification reaction sequences for most of the samples, except for the very Y-rich samples. However, regions with Y_2O_3 were avoided as far as possible during analysis. Another problem was that all the high Y content samples were found to be contaminated with Ta. Subsequently, when the pure Y source material was studied, 1-1.5 μm diameter Ta-rich spheroids were found. Since in energy dispersive x-ray analysis (EDX), the Ni K_α peak overlaps the Ta Lα peak, and the Y Lα peak overlaps with the Ta Mα peak, this made deconvoluting the presence of Ta very difficult, although Ta regions were always very bright in the microstructure in backscattered electron imaging mode (BSE), with Ta (73) having a much higher atomic number than Ni (28), Y (39) or Ru (44).

The EDX analyses for the overall composition of the alloys and the composition of the individual phases of the as-cast samples are given in Table 2, with all compositions in at.%, while the area analyses of the eutectic structures are listed in Table 3. The analyses for the heat treated samples at 1200 °C for 1000 h are given in Table 4.

Unfortunately, the specimens oxidized and disintegrated very soon after scanning electron microscopy (SEM) analysis, and thus most of the samples were not suitable for XRD studies. Even keeping some of the samples in analar grade (AR) methanol and some of the samples in ultra low water (UL) ethanol did not protect the samples. An original sample of composition $\sim Ni_{15}:Ru_{15}:Y_{70}$ (at.%), i.e. high Y content, oxidized almost immediately and was never examined, and Sample 2, $\sim Ni_{54}:Ru_{45}:Y_1$ (at.%), although Y-poor, disintegrated soon after analysis. It was subsequently found that water readily reacts with Y and its compounds to form hydrogen and Y_2O_3,[20] and this is likely to have occurred during metallographic preparation.

3.1 As-Cast Samples

3.1.1 Nominal $\simeq Ni_7:Ru_{72}:Y_{21}$ (at.%), Sample 12. The nominal composition $\sim Ni_7:Ru_{72}:Y_{21}$ (at.%), Sample 12, solidified with (Ru) dendrites in a complex eutectic matrix (Fig. 5). The darkest phase showed a wide range of coring, and formed after the fine univariant binary (Ru) + $\sim YRu_2$ eutectic.

Table 2 Overall compositions of the alloys and phase analyses of the as-cast Ni-Ru-Y alloys (at.%), with values in ranges obtained from cored phases, and the error is associated with both values

Sample no.	Overall analysis Y: Ru:Ni	(Ru) Y: Ru:Ni	~YRu_2 Y: Ru:Ni	~YNi_2 Y: Ru:Ni	(Ni) Y: Ru:Ni	~Y_2Ni_{17} Y: Ru:Ni	~YNi_5 Y: Ru:Ni	~YNi_3 Y: Ru:Ni	~YNi_4 Y: Ru:Ni	~$Y_{44}Ru_{25}$ Y: Ru:Ni	τ	~YNi Y: Ru:Ni	~Y_3Ni_2 Y: Ru:Ni	~Y_3(Ru,Ni) Y: Ru:Ni	~(Y) Y: Ru:Ni
12	20.7 ± 0.2	0.6 ± 1.2	31.6 ± 0.5	29.5 ± 2.7	···	···	···	···	···	···	···	···	···	···	···
	72.0 ± 0.8	97.8 ± 0.5	64.6 ± 0.7	50.7 ± 7.0											
	7.3 ± 0.1	1.6 ± 0.4	3.8 ± 0.6	19.8 ± 8.8											
2	1.0 ± 0.2	0.8 ± 0.4	···	···	0.3 ± 0.1		10.0 ± 1.5	···	···	···	···	···	···	···	···
	44.8 ± 0.7	55.0 ± 2.6			29.3 ± 0.3		11.4 ± 2.1								
	54.2 ± 0.7	44.2 ± 0.3			70.4 ± 0.3		78.6 ± 0.6								
6	19.7 ± 0.2	0.9 ± 0.1	···	23.7 ± 0.3	···	···	···	20.8 ± 0.2	Too small	···	···	···	···	···	···
	41.7 ± 0.3	89.0 ± 1.0		46.1 ± 0.6				22.1 ± 0.6							
	38.6 ± 0.5	10.1 ± 1.0		30.2 ± 0.7				57.1 ± 0.6							
5	14.7 ± 0.2	1.7 ± 0.5	···	···	···	···	15.6 ± 0.2	···	···	···	···	···	···	···	···
	16.3 ± 0.2	71.2 ± 2.0					13.1 ± 0.4								
	69.0 ± 0.2	27.1 ± 1.6					71.3 ± 0.3								
13	11.3 ± 0.3	···	···	···	Too small	···	14.7 to 11.8 ± 2.5	···	···	···	···	···	···	···	···
	12.9 ± 0.2						11.7 to 12.6 ± 2.2								
	75.8 ± 0.3						73.6 to 75.6 ± 2.5								
7	8.6 ± 0.1	···	···	···	Too small	···	10.5 ± 0.2	···	···	···	···	···	···	···	···
	10.3 ± 0.1						8.6 ± 0.3								
	81.1 ± 0.2						80.9 ± 0.2								
8	28.8 ± 0.6	···	···	29.3 ± 2.5	···	···	···	23.7 ± 0.1	···	···	···	···	···	···	···
	10.1 ± 0.1			14.4 ± 2.2				5.5 ± 0.8							
	61.1 ± 0.6			56.3 ± 1.9				70.8 ± 0.8							
16	26.6 ± 0.1	···	···	30.7 ± 3. 0	···	21.2 ± 2.8	···	26.8 ± 0.1	20.1 ± 0.2	···	···	···	···	···	···
	3.1 ± 0.1			3.1 ± 0.1		3.4 ± 0.7		3.9 ± 0.3	2.7 ± 0.1						
	70.3 ± 1.5			66.2 ± 2.3		75.4 ± 2.9		69.3 ± 0.5	77.2 ± 0.2						
3	35.3 ± 0.1	···	32.4 ± 0.3	32.5 ± 0.1	···	···	···	···	···	···	Eut.	···	···	···	···
	45.3 ± 0.3		55.4 ± 2.0	43.7 ± 3.3											
	19.4 ± 0.4		12.2 ± 1.9	23.8 ± 3.2											
11	58.8 ± 0.2	···	···	34.8 ± 5.5	···	···	···	···	···	61.4 ± 0.2	Eut.	···	···	···	···
	31.1 ± 0.2			49.8 ± 4.3						32.1 ± 1.0					
	10.1 ± 0.3			15.4 ± 1.2						6.5 ± 1.0					
17	62.7 ± 0.2	···	···	34.7 ± 0.1	···	···	···	···	···	63.2 ± 0.2	Eut.	···	···	···	···
	31.3 ± 0.5			49.3 ± 1.9						33.0 ± 0.3					
	6.0 ± 0.3			16.0 ± 1.8						3.8 ± 0.3					
18	60.8 ± 0.2			35.6 ± 0.1	···	···	···	···	···	64.7 ± 0.2	55.0 ± 0.3				
	22.6 ± 0.1			48.7 ± 0.4						25.4 ± 0.2	13.9 ± 0.4				
	16.6 ± 0.3			15.7 ± 0.4						9.9 ± 0.6	31.1 ± 0.7				
1	50.0 ± 0.1	···	···	32.9 ± 0.1	···	···	···	···	···	Eut.	Eut.	···	···	···	···
	25.6 ± 0.1			48.3 ± 1.2											
	24.4 ± 0.1			18.8 ± 1.2											

Table 2 continued

Sample no.	Overall analysis Y: Ru:Ni	(Ru) Y: Ru:Ni	~YRu_2 Y: Ru:Ni	~YNi_2 Y: Ru:Ni	(Ni) Y: Ru:Ni	~Y_2Ni_{17} Y: Ru:Ni	~YNi_5 Y: Ru:Ni	~YNi_3 Y: Ru:Ni	~YNi_4 Y: Ru:Ni	~$Y_{44}Ru_{25}$ Y: Ru:Ni	τ	~YNi Y: Ru:Ni	~Y_3Ni_2 Y: Ru:Ni	~Y_3(Ru,Ni) Y: Ru:Ni	~(Y) Y: Ru:Ni
4	43.1 ± 0.3	···	···	31.1 ± 0.1	···	···	···	···	···	···	I. den.	47.3 ± 0.6	···	···	···
	15.6 ± 0.2			35.7 ± 0.8								6.3 ± 0.9			
	41.3 ± 0.2			33.2 ± 0.9								46.4 ± 1.0			
9	58.6 ± 0.2	···	···	···	···	···	···	···	···	···	59.5 ± 0.2	53.5 ± 0.2	···	···	···
	10.7 ± 0.2										13.8 ± 0.5	6.6 ± 2.9			
	30.7 ± 0.2										26.7 ± 0.4	39.9 ± 6.4			
19	65.8 ± 0.4	···	···	···	···	···	···	···	···	···	67.6 ± 1.2	···	58.2 ± 2.2	···	···
	7.7 ± 0.4										10.7 ± 1.5		2.6 ± 0.9		
	26.5 ± 0.6										21.7 ± 2.5		39.2 ± 3.1		
14	78.1 ± 0.2	···	···	···	···	···	···	···	···	···	···	···	···	77.6 to 78.5 ± 0.5	···
	12.1 ± 0.3													14.8-7.9 ± 0.7	
	9.8 ± 0.4													7.6-13.6 ± 0.8	
10	78.3 ± 0.2	···	···	···	···	···	···	···	···	···	···	···	···	76.1 ± 0.4	89.8 ± 6.1
	11.2 ± 0.4													13.3 ± 0.6	3.8 ± 3.1
	10.5 ± 0.6													10.6 ± 0.6	6.4 ± 3.1
15	83.6 ± 0.3	···	···	···	···	···	···	···	···	···	···	···	···	79.7 ± 0.4	83.0 ± 0.4
	6.1 ± 0.3													12.8 ± 0.9	10.5 ± 0.3
	10.3 ± 0.3													7.5 ± 1.1	6.5 ± 0.3

Eut. = eutectic component; I. den. = inner dendrite; and Too small = too small to analyse. τ = $Y_{51}Ru_{15}Ni_{34}$ (at.%)

Table 3 Overall compositions of the univariant binary eutectics in the as-cast Ni-Ru-Y alloys (at.%); sparse eutectic in Sample 4 was not analysed

Sample No.	Overall sample analysis Y: Ru:Ni	Area eutectic analysis			Eutectic components
		Y	Ru	Ni	
12	20.7 ± 0.2 72.0 ± 0.8 7.3 ± 0.1	18.8 ± 1.4	76.1 ± 1.0	5.1 ± 1.0	(Ru) + ~YRu_2
2	1.0 ± 0.2 44.8 ± 0.7 54.2 ± 0.7	8.7 ± 0.4	12.2 ± 0.7	79.1 ± 0.6	(Ni) + ~YNi_5
5	14.7 ± 0.2 16.3 ± 0.2 69.0 ± 0.2	12.5 ± 0.2	22.0 ± 0.4	65.5 ± 0.4	(Ru) + ~YNi_5
13	11.3 ± 0.3 12.9 ± 0.2 75.8 ± 0.3	9.3 ± 0.2	14.8 ± 0.5	75.9 ± 0.6	(Ni) + ~YNi_5
7	8.6 ± 0.1 10.3 ± 0.1 81.1 ± 0.2	6.8 ± 0.3	12.1 ± 0.2	81.1 ± 0.3	(Ni) + ~YNi_5
3	35.3 ± 0.1 45.3 ± 0.3 19.4 ± 0.4	50.7 ± 2.8	14.9 ± 4.3	34.4 ± 7.0	~YNi_2 + τ, $Y_{51}Ru_{15}Ni_{34}$
11	58.8 ± 0.2 31.1 ± 0.2 10.1 ± 0.3	55.2 ± 0.2	20.2 ± 0.3	24.6 ± 0.3	~$Y_{44}Ru_{25}$ + τ, $Y_{51}Ru_{15}Ni_{34}$
17	62.7 ± 0.2 31.3 ± 0.5 6.0 ± 0.3	57.0 ± 1.4	19.3 ± 1.1	23.7 ± 2.2	~$Y_{44}Ru_2$ + τ, $Y_{51}Ru_{15}Ni_{34}$
18	60.8 ± 0.2 22.6 ± 0.1 16.6 ± 0.3	58.6 ± 0.5	18.3 ± 0.4	23.1 ± 0.7	~$Y_{44}Ru_{25}$ + τ, $Y_{51}Ru_{15}Ni_{34}$
1	50.0 ± 0.1 25.6 ± 0.1 24.4 ± 0.1	54.6 ± 0.2	18.6 ± 1.7	26.8 ± 0.3	~$Y_{44}Ru_{25}$ + τ, $Y_{51}Ru_{15}Ni_{34}$
10	78.3 ± 0.2 11.2 ± 0.4 10.5 ± 0.6	81.9 ± 1.0	8.7 ± 0.8	9.4 ± 0.3	~Y_3(Ru,Ni) + (Y)
15	83.6 ± 0.3 6.1 ± 0.3 10.3 ± 0.3	79.0 ± 0.7	12.4 ± 0.5	8.6 ± 0.3	~Y_3(Ru,Ni) + (Y)

The solidification reactions were:

$$L \rightarrow (Ru)$$

$$L \rightarrow (Ru) + \sim YRu_2$$

$$L + (Ru) + \sim YRu_2 \rightarrow \sim YNi_2$$

where the latter was a ternary peritectic reaction.

3.1.2 Nominal ≃Ni_{54}:Ru_{45}:Y_1 (at.%), Sample 2. The nominal ~Ni_{54}:Ru_{45}:Y_1 (at.%) sample solidified with very cored (Ru) dendrites, followed by very clear peritectially-formed (Ni) (Fig. 6). There were very small areas of a globular (Ni) + ~YNi_5 eutectic. These were much too fine to analyse the components accurately (and even the overall composition of the eutectic were just on the limit for reasonable analyses).

The solidification sequence was:

$$L \rightarrow (Ru)\,(cored)$$

$$L + (Ru) \rightarrow (Ni)$$

$$L \rightarrow (Ni) + \sim YNi_5.$$

3.1.3 Nominal Ni_{38}:Ru_{42}:Y_{20} (at.%), Sample 6. The Ni_{38}:Ru_{42}:Y_{20} (at.%) sample (Sample 6) had small primary (Ru) dendrites (Fig. 7). Next in the solidification sequence

Table 4 Overall compositions of the alloys and phase analyses of the Ni-Ru-Y alloys annealed at 1200 °C (at.%); samples with different regions are given increasing numbers working inwards

Sample No.	Overall analysis Y: Ru:Ni	(Ru) Y: Ru:Ni	~YRu_2 Y: Ru:Ni	~YNi_2 Y: Ru:Ni	~YNi_5 Y: Ru:Ni	~YNi_3 Y: Ru:Ni	~YNi_4 Y: Ru:Ni
6H-1	12.4 ± 0.4	0.6 ± 0.1	···	···	16.0 ± 0.1	···	···
	24.8 ± 1.1	92.1 ± 0.7			8.0 ± 0.1		
	62.8 ± 0.9	7.3 ± 0.7			76.0 ± 0.2		
6H-2	16.1 ± 0.6	0.7 ± 0.2	···	···	···	···	21.5 ± 0.2
	31.7 ± 2.0	91.0 ± 1.0					12.4 ± 0.4
	52.2 ± 1.5	8.3 ± 1.1					66.1 ± 0.4
6H-3	18.1 ± 0.5	0.8 ± 0.3	···	···	···	23.9 ± 0.3	···
	31.9 ± 1.6	91.0 ± 2.1				17.9 ± 0.4	
	50.0 ± 1.1	8.2 ± 2.0				58.2 ± 0.2	
6H-4	21.3 ± 0.5	0.7 ± 0.3	···	···	···	26.7 ± 0.2	···
	38.4 ± 0.9	92.0 ± 1.1				28.7 ± 0.2	
	40.3 ± 0.5	7.3 ± 1.0				44.6 ± 0.3	
5H	13.0 ± 0.5	0.6 ± 0.1	···	···	15.4 ± 0.6	···	···
	13.0 ± 0.5	85.2 ± 0.7			6.5 ± 0.5		
	74.0 ± 1.0	14.2 ± 0.8			78.1 ± 0.3		
3H-1	35.7 ± 0.7	1.8 ± 0.3	···	35.4 ± 0.5	···	···	···
	48.0 ± 0.2	93.6 ± 0.9		47.1 ± 0.8			
	16.3 ± 0.5	4.6 ± 0.7		17.5 ± 1.2			
3H-2	32.1 ± 0.5	···	···	32.2 ± 0.2	···	···	···
	48.8 ± 2.5			48.3 ± 0.2			
	19.1 ± 2.1			19.5 ± 0.3			
3H-3	12.4 ± 1.6	1.0 ± 0.6	···	31.3 ± 0.3	···	···	···
	82.9 ± 2.0	97.8 ± 0.6		59.0 ± 0.6			
	4.7 ± 0.4	1.2 ± 0.2		9.7 ± 0.6			
3H-4	33.1 ± 1.2	1.4 ± 0.4	30.3 ± 0.7	36.7 ± 0.4	···	···	···
	56.6 ± 1.7	94.6 ± 0.7	61.0 ± 0.8	50.0 ± 0.2			
	10.3 ± 1.1	4.0 ± 0.6	8.7 ± 0.2	13.3 ± 0.1			
1H	34.2 ± 1.3	···	···	34.0 ± 0.2	···	27.3 ± 0.2	···
	35.6 ± 3.7			36.9 ± 0.2		26.8 ± 2.0	
	30.2 ± 4.0			29.1 ± 0.3		45.9 ± 2.0	
4H	31.7 ± 1.7	···	···	32.6 ± 0.2	···	27.4 ± 0.2	···
	22.1 ± 3.2			31.9 ± 2.2		14.9 ± 0.1	
	46.2 ± 4.5			35.5 ± 2.4		57.7 ± 0.3	

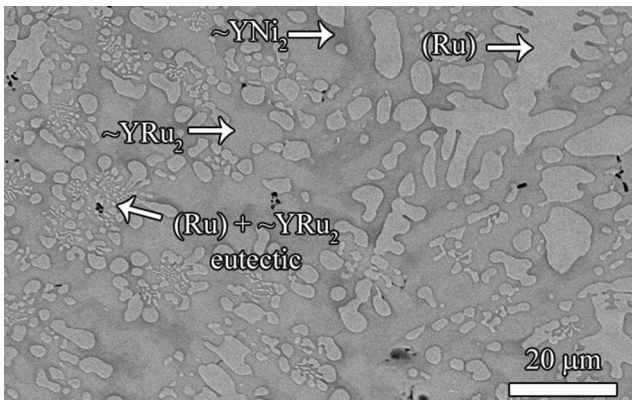

Fig. 5 Scanning electron microscope backscattered electron image (SEM-BSE) image of as-cast nominal Ni_7:Ru_{72}:Y_{21} (at.%) (Sample 12), showing (Ru) dendrites (light), (Ru) + ~YRu_2 (dark) eutectic structure and ~YNi_2 (medium)

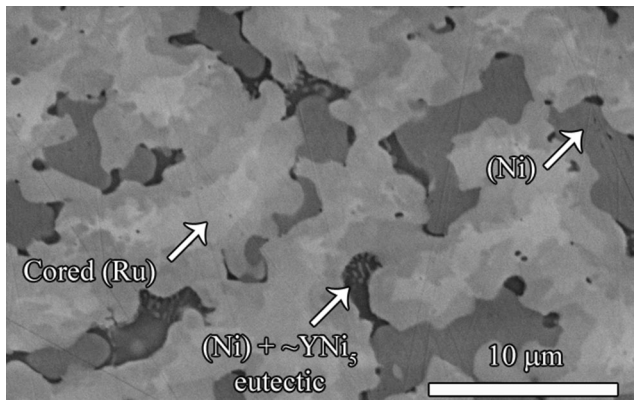

Fig. 6 SEM-BSE image of as-cast nominal Ni_{54}:Ru_{45}:Y_1 (at.%) (Sample 2), showing very cored (Ru) dendrites (light), (Ni) (medium) and small areas of (Ni) (discrete) + YNi_5 (dark) eutectic structure

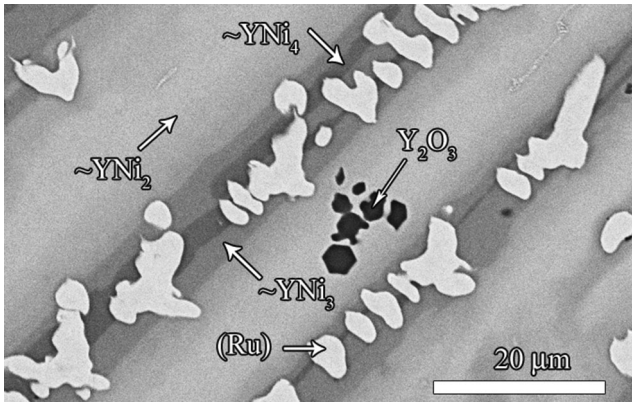

Fig. 7 SEM-BSE image of as-cast nominal Ni_{38}:Ru_{42}:Y_{20} (at.%) (Sample 6), showing primary (Ru) dendrites (very light), ~YNi_2 needles (light), ~YNi_3 (medium) and ~YNi_4 (dark). The very darkest phase is Y_2O_3, or holes left after it was removed on sample preparation

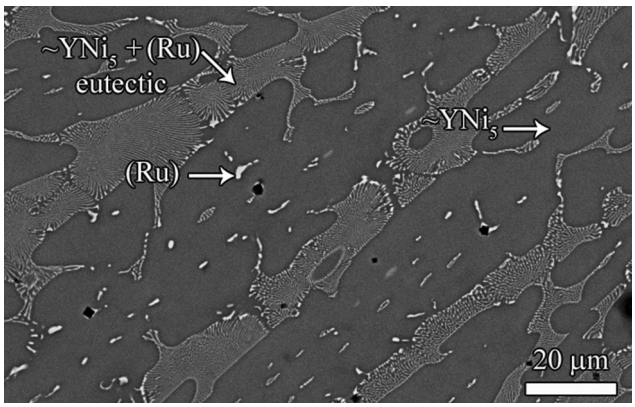

Fig. 8 SEM-BSE image of as-cast nominal Ni_{69}:Ru_{16}:Y_{15} (at.%) (Sample 5), showing ~YNi_5 (dark dendrites) and ~YNi_5 + (Ru) (light) eutectic structure

were two peritectic reactions forming large needles of ~YNi_2 (sometimes pushing the dendrites aside), and ~YNi_3. The ~YNi_2 phase had a much wider solubility than in the redrawn isothermal sections.[9,10] At higher magnifications, another phase was observed, and all phases had distinct boundaries (Fig. 7), indicating distinct phases rather than coring. The small dark phase areas of ~YNi_4 would have meant that the EDX analyses were affected by the surrounding phases, so their analyses are not reported. There were also lighter contrast regions within the ~YNi_2 needles, assumed to be ~YNi_2 with higher Ru content, which solidified before the ~YNi_2 with lower Ru content, with the lightest being remnant (Ru) dendrites (i.e. an incomplete peritectic reaction). The ~YNi_2 solidified at a higher temperature than in the Ni-Y binary, because of the higher Ru content, and the direction of slope of the liquidus is consistent with the phase contrasts and analyses (albeit not accurate).

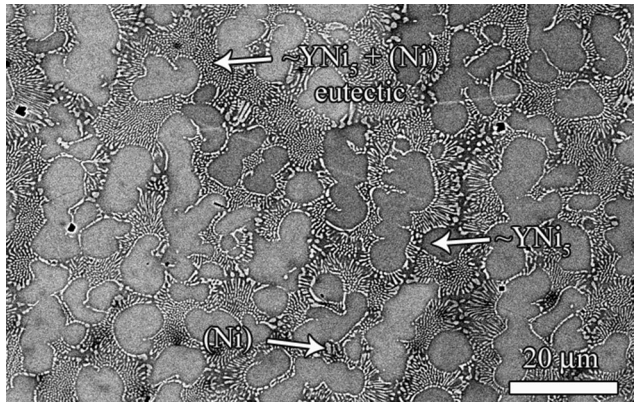

Fig. 9 SEM-BSE image of as-cast nominal Ni_{76}:Ru_{13}:Y_{11} (at.%) (Sample 13), showing ~YNi_5 dendrites (dark) and ~YNi_5 + (Ni) (light) eutectic structure

Thus, the deduced solidification reactions are:

$$L \rightarrow (Ru)$$

$$L + (Ru) \rightarrow \sim YNi_2$$

$$L + \sim YNi_2 \rightarrow \sim YNi_3$$

$$L + \sim YNi_3 \rightarrow YNi_4.$$

3.1.4 Nominal Ni_{69}:Ru_{16}:Y_{15} (at.%), Sample 5. Nominal Ni_{69}:Ru_{16}:Y_{15} (at.%) (Sample 5) was mostly dendrites of ~YNi_5 with a fine lamellar eutectic structure comprising ~YNi_5 and (Ru) (Fig. 8). The light phase was much too fine for accurate analysis, which was shown by the large errors (up to ±2.0 at.%), and should have had a much higher Ru content.

The solidification sequence was:

$$L \rightarrow \sim YNi_5$$

$$L \rightarrow \sim YNi_5 + (Ru).$$

3.1.5 Nominal ≃Ni_{76}:Ru_{13}:Y_{11} (at.%), Sample 13. Nominal ~Ni_{76}:Ru_{13}:Y_{11} (at.%) (Sample 13) had ~YNi_5 dendrites of slightly different BSE contrasts and compositions, and a fairly coarse lamellar eutectic structure (Fig. 9). There was also fine precipitation in the dendrites. The dendrite analyses were similar, with the differences deriving from different local dendrite compositions on solidification and varying amounts of precipitation within. These effects were caused by the ~YNi_5 phase having a very sloping solvus, so the lighter dendrites had slightly more Ru and Y, which would account for the large errors. Both of the eutectic components were too fine to accurately analyse individually, but the overall analysis of the univariant binary eutectic was obtained (Table 2).

The solidification sequence was:

$$L \rightarrow \sim YNi_5$$

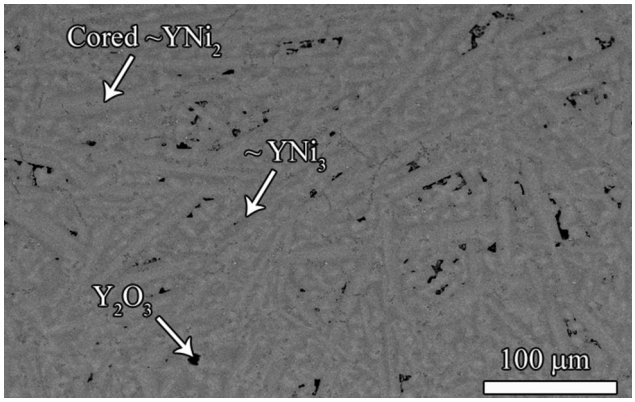

Fig. 10 Low magnification SEM-BSE image of as-cast nominal Ni_{61}:Ru_{10}:Y_{29} (Sample 8), showing cored ~YNi_2 dendrites (light) and ~ YNi_3 (medium), with Y_2O_3 particles (dark)

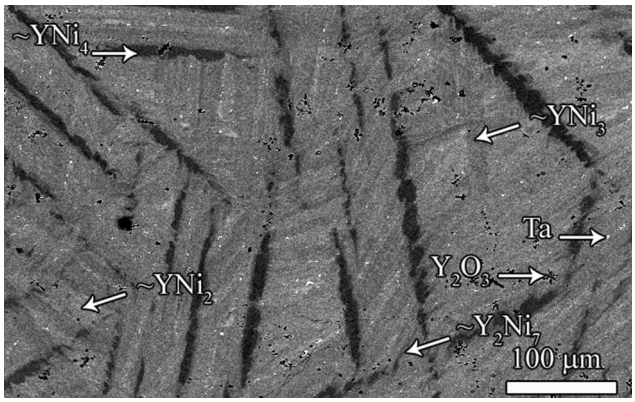

Fig. 11 SEM-BSE image of as-cast nominal Ni_{70}:Ru_3:Y_{27} (at.%) (Sample 16), showing ~YNi_4 (dark), ~Y_2Ni_7 (medium dark), ~YNi_3 (medium), and ~YNi_2 (light). Darkest regions are holes where Y_2O_3 was removed on sample preparation, and the very lightest regions are contamination from Ta

$$L \rightarrow\sim YNi_5 + (Ni).$$

3.1.6 Nominal ≃Ni_{81}:Ru_{10}:Y_9 (at.%), Sample 7. Nominal ~Ni_{81}:Ru_{10}:Y_9 (at.%) (Sample 7) was similar to ~Ni_{76}:Ru_{13}:Y_{11} (at.%) (Sample 13), with the same solidification sequence, and precipitation within the dendrites. The true dendrite phase composition should be extrapolated away from (Ni) (which precipitated within), giving the phase to be ~YNi_5 (also confirming the ~YNi_5 phase in Sample 2).

3.1.7 Nominal ≃Ni_{61}:Ru_{10}:Y_{29} (at.%), Sample 8. In nominal ~Ni_{61}:Ru_{10}:Y_{29}, the darkest phase was Y_2O_3 (Fig. 10) and in some regions there was high porosity associated with the last phase to solidify. The ~YNi_2 needles formed first, followed by ~YNi_3, and distinct interfaces between ~YNi_2 and ~YNi_3 were seen at higher magnification.

Ignoring the Y_2O_3, the solidification sequence was:

$$L \rightarrow\sim YNi_2(\text{cored})$$

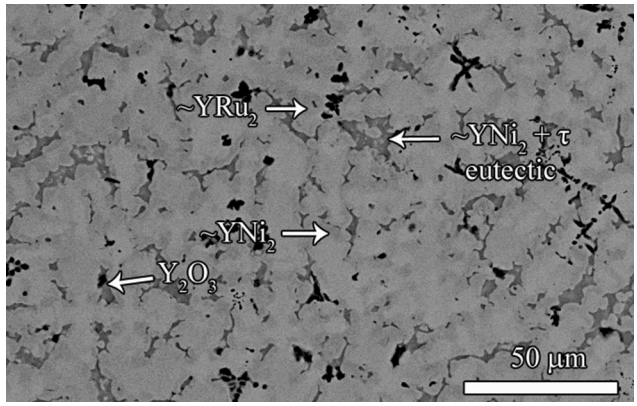

Fig. 12 SEM-BSE image of as-cast nominal Ni_{20}:Ru_{45}:Y_{35} (at.%) (Sample 3), showing Y_2O_3 (dark), ~YRu_2 inner dendrites (light), ~YNi_2 outer dendrites (slightly darker) in a sparse eutectic structure of ~YNi_2 + τ (medium). The very darkest regions are holes left by Y_2O_3 falling out

$$L + \sim YNi_2 \rightarrow\sim YNi_3.$$

3.1.8 Nominal Ni_{70}:Ru_3:Y_{27} (at.%), Sample 16. Ignoring the light contrast contamination which filled some of the holes after polishing nominal ~Ni_{70}:Ru_3:Y_{27} (at.%) (Sample 16) and the prior Y_2O_3 phase, most of which had fallen out during sample polishing, leaving holes, there were four phases present (Fig. 11). The first phase to form, ~YNi_4, could have been dendritic in morphology, although the subsequent peritectic reaction removed most of the outline, leaving an irregular needle-like appearance. The phase identification was achieved by comparison to the isothermal section of Sokolovskaya et al.,[9] and by assuming that the binary Ni-Y phases extended into the ternary at constant Y content. The solidification sequence agreed with the peritectic cascade of phases reported in the Ni-Y binary,[5] and ignoring Y_2O_3, was:

$$L \rightarrow\sim YNi_4$$

$$L + \sim YNi_4 \rightarrow\sim Y_2Ni_7$$

$$L + \sim Y_2Ni_7 \rightarrow\sim YNi_3$$

$$L + \sim YNi_3 \rightarrow\sim YNi_2.$$

The ~Y_2Ni_7 and ~YNi_2 phases were too small to analyse accurately, giving large errors, and the analyses were made more Ni-rich by the surrounding higher Ni-content phases.

3.1.9 Nominal Ni_{19}:Ru_{46}:Y_{35} (at.%), Sample 3. There were some oxide particles in the nominal ~Ni_{19}:Ru_{46}:Y_{35} (at.%) alloy (Sample 3), and the main dendrites had an inner composition of Y_{33}:Ru_{55}:Ni_{12} (at.%), and an outer composition of ~Y_{24}:Ru_{44}:Ni_{32} (at.%). There were minor amounts of a two-phase interdendritic region of overall composition ~Y_{51}:Ru_{15}:Ni_{34} (Fig. 12), where the contrast of one phase was similar to the outer dendrite. In some places, the

dendrites appeared cored, whereas in others, there was a distinct interface between the ~Y_{33}:Ru_{55}:Ni_{12} and ~Y_{24}:Ru_{44}:Ni_{32} (at.%). Both of these compositions, even with the relatively high errors (±3 at.% for the most Ni-rich component, and ±2 at.% for the most Ru-rich component) were on the ~YRu_2 to ~YNi_2 transect, and fairly close to the limits of the ~YRu_2 and ~YNi_2 phases.[7,9] The high errors in Ni and Ru contents are consistent with coring in the Ni and Ru directions, and the low errors in Y are consistent with the phases having constant Y content. In the absence of good x-ray data, the phases could only be deduced by morphology and composition. The ~YNi_2 phase solidified as facetted dendrites with 48.3 at.% Ru (Sample 1) (Fig. 16) and 35.7 at.% Ru (Sample 4) (Fig. 17), facetted crystals with 49.8 at% Ru (Sample 11) (Fig. 13), needles as a secondary phase with 46.1 at.% Ru (Sample 6) (Fig. 7), and needles then dendrites with 14.4 at.% Ru (Sample 8) (Fig. 10). Thus, for higher Ru contents, ~YNi_2 tended to solidify with a more facetted morphology, and with lower Ru contents, as dendrites. Here, the outer phase comprised 43.7 at.% Ru, which should have given a more facetted appearance, if it was ~YNi_2. However, the phase was growing on a fair proportion of pre-existing ~YRu_2, and so would have taken that shape initially. Thus, the two compositions and different contrasts were deduced to be inner dendrites of ~YRu_2 (of ~55.4 at.% Ru). Since the analyses of the interdendritic region were actually of a sparse eutectic structure, which comprised mainly the darker component (lower atomic number contrast), the analysed composition of that component must lie near the univariant binary eutectic. However, since the overall analysis of this eutectic had large error bars (due to only small areas being available for analysis, and its univariant quality) and were near to the reported composition of ~$Y_5Ru_2Ni_2$,[9] which here is called τ, (~$Y_{51}Ru_{15}Ni_{34}$ (at.%)), the darker component was taken to be τ. Comparison with the isothermal section[9] shows that the overall composition of the univariant binary eutectic, ~Y_{51}:Ru_{15}:Ni_{34}, was in the two-phase region of τ + ~YNi, but the sparse component had the same contrast as ~YNi_2, and so is taken to be this phase.

Ignoring the Y_2O_3 phase, the sequence on solidification was:

$$L \rightarrow\sim YRu_2$$

$$L + \sim YRu_2 \rightarrow\sim YNi_2$$

$$L \rightarrow\sim YNi_2 + \tau, \sim Y_{51}Ru_{15}Ni_{34}.$$

3.1.10 Nominal ≃Ni_{10}:Ru_{31}:Y_{59} (at.%), Sample 11. The microstructure of Sample 11, nominal ~Ni_{10}:Ru_{31}:Y_{59} (at.%), was complex and there appeared to be two different primary phases, ignoring Y_2O_3. The yttrium oxide solidified first and acted as a nucleation site locally for either of the next phases, showing that the boundary between the ~YNi_2 and ~$Y_{44}Ru_{25}$ liquidus surfaces was very close to the overall composition of the sample. In some places, ~YNi_2 formed on the oxide as regular, almost square, facetted blocks (top left of Fig. 13), and next, facetted ~$Y_{44}Ru_{25}$ formed, with a final univariant binary eutectic reaction. The oxide was ignored for phase diagram considerations. The EDX analyses (Table 2) had unacceptably high errors for ~YNi_2, although the light phase appeared large enough to analyse without collecting any x-rays from the surrounding phases. This would be consistent with a wider phase field in the Y direction and coring on solidification, i.e. the Ru direction. The overall composition of the univariant binary eutectic was close to the ternary ~$Y_5Ru_5Ni_2$ phase,[9] and one eutectic phase was clearly ~$Y_{44}Ru_{25}$, as it was associated with the facetted blocks. The composition of the second eutectic phase was roughly estimated by extrapolating from the known (by EDX analysis) eutectic phase, ~$Y_{44}Ru_{25}$, through the overall composition of the eutectic, considering the proportions of the eutectic phases, to give τ, ~$Y_{51}Ru_{15}Ni_{34}$. (This was very approximate, because it assumed the tie triangle of the univariant binary eutectic was a straight line.) The ~YNi_2 phase also had another morphology, which was more irregular (centre of Fig. 13), but still facetted, and in this morph, it was associated with the univariant binary eutectic. This was deduced to be from mainly solid state precipitation (which occurred after solidification was complete), after forming as a coarse eutectic structure with ~$Y_{44}Ru_{25}$, and then the final, much finer, ~$Y_{44}Ru_{25}$ + τ eutectic structure. This indicates that the ~$Y_{44}Ru_{25}$ solvus is sloping with temperature, allowing the ~YNi_2 to be precipitated subsequently in such a coarse morphology.

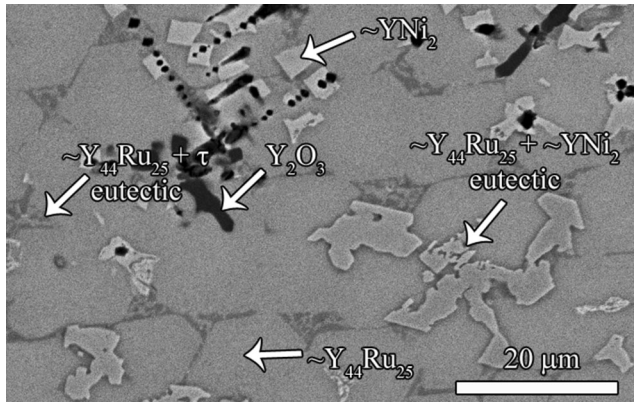

Fig. 13 SEM-BSE image of as-cast nominal Ni_{10}:Ru_{31}:Y_{59} (at.%) (Sample 11), showing Y_2O_3 dendrites (very dark), facetted YNi_2 (light) and $Y_{44}Ru_{25}$ facetted dendrites (medium contrast) with a coarse ~$Y_{44}Ru_{25}$ + ~YNi_2 eutectic structure, and fine ~$Y_{44}Ru_{25}$ + τ, ~$Y_{51}Ru_{15}Ni_{34}$ (medium dark) eutectic structure

Ignoring the Y_2O_3 phase, which is not part of the true solidification sequence for this composition, the solidification sequence for the regions where very regular ~YNi_2 formed (i.e. locally on that liquidus surface) is:

(1)

$$L \rightarrow\sim YNi_2$$

$$L \rightarrow\sim Y_{44}Ru_{25} + \sim YNi_2 \text{(small amounts, which subsequently coarsened in the solid state)}$$

$$L \rightarrow\sim Y_{44}Ru_{25} + \tau, \sim Y_{51}Ru_{15}Ni_{34}.$$

(2)

Alternatively, most of the sample solidified by:

$$L \rightarrow\sim Y_{44}Ru_{25}$$

$$L \rightarrow\sim Y_{44}Ru_{25} + \sim YNi_2 \text{(small amounts, which subsequently coarsened in the solid state)}$$

$$L \rightarrow\sim Y_{44}Ru_{25} + \tau, \sim Y_{51}Ru_{15}Ni_{34}.$$

The average overall composition for the regions of solidification reaction 1 was 5.5 ± 0.2 Ni, 31.8 ± 0.6 Ru, 62.7 ± 0.5 1 Y (at.%), with ~YNi_2 solidifying first, whereas the average overall composition for the regions of solidification reaction 2 was 6.4 ± 0.5 Ni, 31.9 ± 0.6 Ru, 61.8 ± 1.1 Y (at.%), with ~$Y_{44}Ru_{25}$ solidifying first. Thus, the ~YNi_2 and ~$Y_{44}Ru_{25}$ liquidus surface boundary runs between these different local overall compositions. The solidification reaction that occurred only locally showed that the peritectic reaction forming ~$Y_{44}Ru_{25}$ from ~YNi_2 changed to a univariant binary eutectic at lower temperatures.

3.1.11 Nominal Ni_6:Ru_{31}:Y_{63} (at.%), Sample 17. Nominal Ni_6:Ru_{31}:Y_{63} (at.%) (Sample 17) was very similar to Sample 11, with the same phases and mostly the same morphologies, except that locally, ~YNi_2 formed definite facetted dendrites and hollow hexagons (Fig. 14). This confirmed that the boundary between the ~YNi_2 and ~$Y_{44}Ru_{25}$ liquidus surfaces must lie between these two compositions. The major primary phase was ~$Y_{44}Ru_{25}$ and the solidification reaction was the same as Reaction 2 for Sample 11.

3.1.12 Nominal Ni_{16}:Ru_{23}:Y_{61} (at.%), Sample 18. Nominal Ni_{16}:Ru_{23}:Y_{61} (at.%) (Sample 18) had a high proportion of Y_2O_3, but the true primary phase (of the Ni-Ru-Y system) was ~YNi_2, which formed as facetted dendrites (Fig. 15). The next phase was ~$Y_{44}Ru_{25}$, which formed long needles, and a univariant binary eutectic formed last. Although the morphology of the ~$Y_{44}Ru_{25}$ phase and ~$Y_{44}Ru_{25}$ + τ eutectic structure appeared different in Samples 11 and 17, this is because the overall compositions of the univariant binary eutectic and phase proportions were different.

The solidification reactions were (ignoring the oxides):

$$L \rightarrow\sim YNi_2$$

$$L + \sim YNi_2 \rightarrow\sim Y_{44}Ru_{25}$$

$$L \rightarrow\sim Y_{44}Ru_{25} + \tau, \sim Y_{51}Ru_{15}Ni_{34}.$$

3.1.13 Nominal Ni_{24}:Ru_{26}:Y_{50} (at.%), Sample 1. The nominal Ni_{24}:Ru_{26}:Y_{50} (at.%) alloy (Sample 1) comprised primary ~YNi_2 as facetted dendrites in a univariant binary eutectic (Fig. 16; Table 2). Both of the eutectic phases were too small to accurately analyse individually, without collecting x-rays from the neighbouring phases. Comparison to the other univariant binary eutectics in the same region (Samples 1, 3, 11, 17 and 18) showed that the morphologies of these eutectics were similar, except for that of Sample 3, which was more

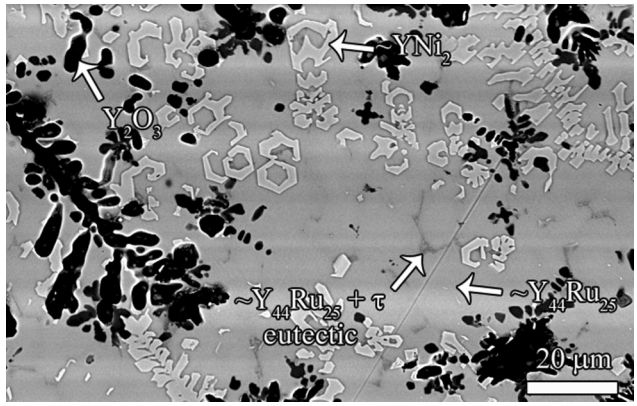

Fig. 14 SEM-BSE image of as-cast nominal Ni_6:Ru_{31}:Y_{63} (at.%) (Sample 17), showing Y_2O_3 dendrites (very dark), hollow hexagonal sections and facetted ~YNi_2 dendrites (light) and less-facetted coarse ~$Y_{44}Ru_{25}$ dendrites (medium contrast) with a small amount of fine ~$Y_{44}Ru_{25}$ + τ, ~$Y_{51}Ru_{15}Ni_{34}$ (medium dark) eutectic structure

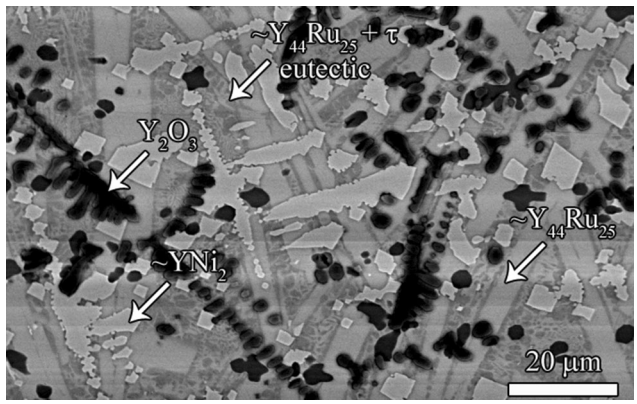

Fig. 15 SEM-BSE image of as-cast nominal Ni_{16}:Ru_{23}:Y_{61} (at.%) (Sample 18), showing Y_2O_3 dendrites (very dark), facetted ~YNi_2 dendrites (light) and ~$Y_{44}Ru_{25}$ needles (medium contrast) with ~$Y_{44}Ru_{25}$ + τ, ~$Y_{51}Ru_{15}Ni_{34}$ (medium dark) eutectic structure

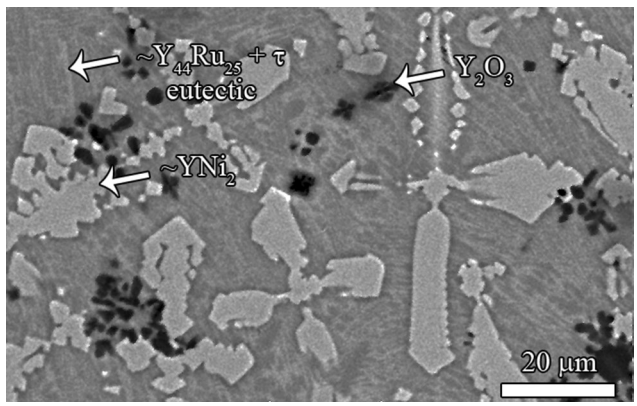

Fig. 16 SEM-BSE image of as-cast nominal Ni_{24}:Ru_{26}:Y_{50} (at.%) (Sample 1), showing ~YNi_2 facetted dendrites (light) in a ~$Y_{44}Ru_{25}$ (medium) + τ, ~$Y_{51}Ru_{15}Ni_{34}$ (medium dark) eutectic structure, with the darkest phase being yttrium oxide

sparse, indicating that Samples 1, 11, 17 and 18 had the same univariant binary eutectic. This gave the eutectic here as $\sim Y_{44}Ru_{25} + \tau$, $\sim Y_{51}Ru_{15}Ni_{34}$, whereas Sample 3 had a different univariant binary eutectic: $\sim YNi_2 + \tau$, $\sim Y_{51}Ru_{15}Ni_{34}$.

Ignoring the oxides (which formed first, and are not part of the ternary system), the deduced solidification sequence was:

$$L \rightarrow \sim YNi_2$$

$$L + \sim YNi_2 \rightarrow \sim Y_{44}Ru_{25} + \tau, \sim Y_{51}Ru_{15}Ni_{34}.$$

The latter was a ternary invariant transition reaction.

3.1.14 Nominal Ni_{41}:Ru_{16}:Y_{43} (at.%), Sample 4. The alloy of nominal composition Ni_{41}:Ru_{16}:Y_{43} (Sample 4) had facetted and apparently cored dendrites of $\sim YNi_2$ (Fig. 17). However, if cored, the insides of the dendrites should have been lighter in BSE contrast, because they should have been more Ru-rich than the outer region. Since the dendrite inners were actually darker, they were deduced to be a phase with less Ru than $\sim YNi_2$, and thus τ, $\sim Y_{51}Ru_{15}Ni_{34}$, since the alternative, $\sim$YNi, formed subsequently. Surrounding the facetted dendrites was a sparse univariant binary eutectic with $\sim$YNi as the major component, and the minor component was deduced by contrast to be $\sim YNi_2$.

Ignoring the oxide phases, the solidification sequence was:

$$L \rightarrow \tau, \sim Y_{51}Ru_{15}Ni_{34}$$

$$L + \tau, \sim Y_{51}Ru_{15}Ni_{34} \rightarrow \sim YNi_2$$

$$L \rightarrow \sim YNi_2 + \sim YNi.$$

3.1.15 Nominal Ni_{31}:Ru_{11}:Y_{58} (at.%), Sample 9. The microstructure of nominal Ni_{31}:Ru_{11}:Y_{58} (at.%) (Sample 9) (Fig. 18) shows small, dark oxide dendrites, some of which were larger than usual, which had mostly been removed by polishing (being more brittle). There were medium grey contrast $\sim$YNi dendrites which sometimes formed on the oxide dendrites, followed by the light τ matrix. The errors for the EDX analyses, especially for the $\sim$YNi and oxide phases, were unacceptably high, but their areas were small and the beam presumably spread more than expected.

The solidification sequence was:

$$L \rightarrow \sim YNi$$

$$L + \sim YNi \rightarrow \tau, \sim Y_{51}Ru_{15}Ni_{34}.$$

3.1.16 Nominal Ni_{26}:Ru_8:Y_{66} (at.%), Sample 19. Apart from the usual small Y_2O_3 dendrites, nominal Ni_{26}:Ru_8:Y_{66} (at.%) (Sample 19) comprised a coarse globular eutectic structure, with the lighter component, τ, $\sim Y_{51}Ru_{15}Ni_{34}$ almost appearing dendritic (Fig. 19). However, the fine scale of the morphology showed that this was a univariant binary eutectic, with very small dendrites of τ, $\sim Y_{51}Ru_{15}Ni_{34}$

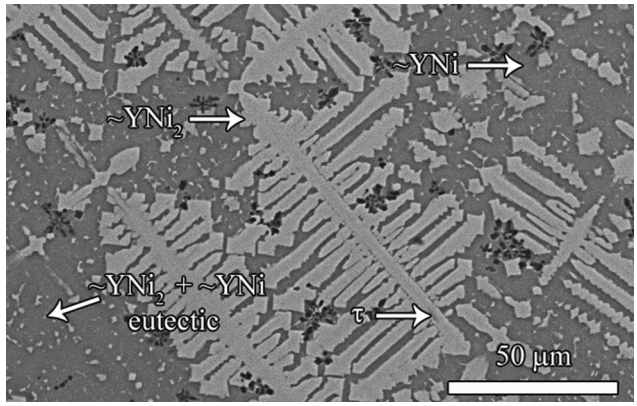

Fig. 17 SEM-BSE image of as-cast nominal Ni_{41}:Ru_{16}:Y_{43} (at.%) (Sample 4), showing inner dendrites of τ, $\sim Y_{51}Ru_{15}Ni_{34}$ (medium) surrounded by outer $\sim YNi_2$ dendrites (light), in a $\sim YNi_2$ + $\sim$YNi (dark) eutectic structure, with darkest phase being yttrium oxide

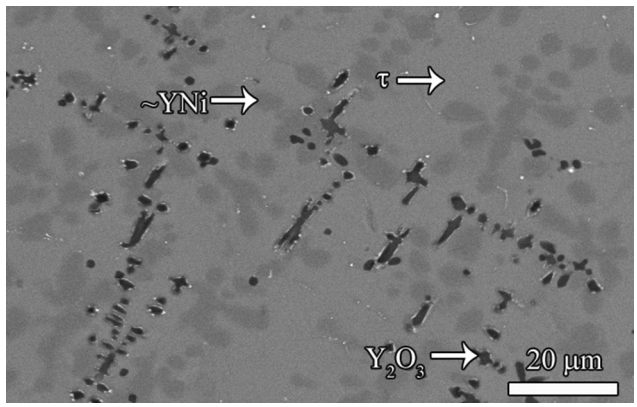

Fig. 18 SEM-BSE image of as-cast nominal Ni_{31}:Ru_{11}:Y_{58} (at.%) (Sample 9), showing $\sim$YNi dendrites (medium) and τ, $\sim Y_{51}Ru_{15}Ni_{34}$ (light), with the very dark dendrites being holes left by the removal of Y_2O_3 during sample preparation

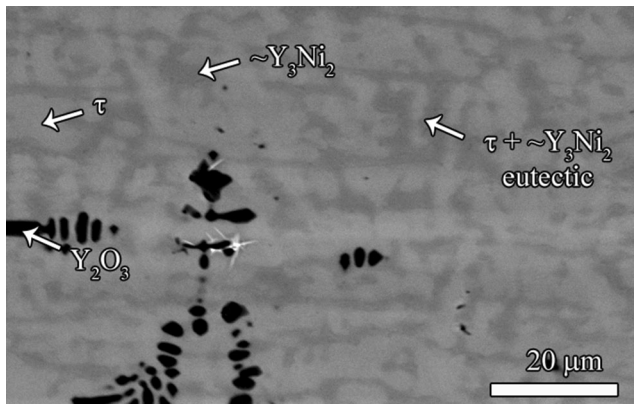

Fig. 19 SEM-BSE image of as-cast nominal Ni_{26}:Ru_8:Y_{66} (at.%) (Sample 19), showing τ, $\sim Y_{51}Ru_{15}Ni_{34}$ dendrites (light) in a globular τ, $\sim Y_{51}Ru_{15}Ni_{34}$ (light) + $\sim Y_3Ni_2$ (medium) eutectic structure, with very dark Y_2O_3

occasionally solidifying before the eutectic. Thus, the alloy composition was just on the τ-rich side of the τ, $\sim Y_{51}Ru_{15}Ni_{34}$ + $\sim Y_3Ni_2$ univariant binary eutectic valley, and the sample mostly solidified to the globular eutectic.

The solidification sequence was:

$$L \rightarrow \tau, \sim Y_{51}Ru_{15}Ni_{34}(\text{locally, in small regions})$$

$$L \rightarrow \tau \sim Y_{51}Ru_{15}Ni_{34} + \sim Y_3Ni_2.$$

3.1.17 Nominal Ni_{10}:Ru_{12}:Y_{78} (at.%), Sample 14. Unfortunately, the sample of nominal composition Ni_{10}:Ru_{12}:Y_{78} (at.%) (Sample 14) because it is Y-rich was noticeably contaminated by tantalum, which formed almost pure (Ta) dendrites on the small Y_2O_3 dendrites. The sample also formed a scale after manufacture and while in methanol. Although difficult to determine, because of the overlapping of the Ni and Y x-ray peaks with those of Ta, it was deduced that there was no Ta in the matrix (with the reasons given in the discussion).

It was difficult to differentiate whether the rest of the microstructure was two separate phases, or coring, but the first component to form (after Y_2O_3 and (Ta)) was the lighter component, originally assumed to be $\sim Y_3Ru$. The darker "interdendritic" regions were of the composition of $\sim Y_3Ni$ at 600 °C,[8,9] and there was no discernable interface between them, indicating coring of an isomorphous phase, $\sim Y_3(Ru,Ni)$, rather than the two separate binary phases.

Thus, the solidification in the ternary was:

$$L \rightarrow \sim Y_3(Ru, Ni)\ (\text{cored and isomorphous}).$$

3.1.18 Nominal Ni_{10}:Ru_{11}:Y_{79} (at.%), Sample 10. Sample 10, nominal Ni_{10}:Ru_{11}:Y_{79} (at.%), was the only sample to have two different contrast dendrites of Y_2O_3 and (Y), and these are thought to be (Y) in two different stages of oxidation (although these were a minor portion of the sample). There was also quite high Ta contamination, because of sample had a higher Y content. The major phase was dendritic $\sim Y_3(Ru,Ni)$, with a comparable solubility for Ni with that reported at 600 °C.[9] The rest of the sample was an irregular $\sim Y_3(Ru,Ni)$ + (Y) univariant binary eutectic viewed at different orientations, similar to that in Fig. 20, consistent with the eutectic in the Ru-Y binary.[5] The (Y) in the eutectic structure had a different morphology from the small Y_2O_3 dendrites, as though it was still being oxidised and falling out. There were also holes where the Y_2O_3 had been removed during sample preparation.

Ignoring the obvious Y_2O_3 and the Ta contamination associated with Y, the solidification sequence was:

$$L \rightarrow \sim Y_3(Ru, Ni)$$

$$L \rightarrow \sim Y_3(Ru, Ni) + (Y).$$

3.1.19 Nominal Ni_{10}:Ru_6:Y_{84} (at.%), Sample 15. The sample of composition Ni_{10}:Ru_6:Y_{84} (at.%) was also contaminated with Ta, but once again, the Ta was only found as small pure Ta particles in the sample, and did not dissolve in any of the other phases. This sample also formed

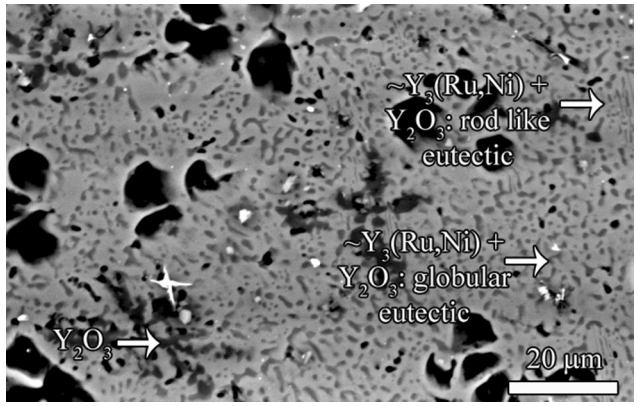

Fig. 20 SEM-BSE image of as-cast nominal Ni_{14}:Ru_8:Y_{78} (at.%) (Sample 15), showing two apparent eutectic structure morphologies (actually different orientations) of $\sim Y_3(Ru,Ni)$ (light) + Y_2O_3 (dark): globular (mostly) and rod-like, and Y_2O_3

a scale after manufacture, and in methanol, and to a greater extent than Sample 14. There were holes where Y_2O_3 had been pulled out during sample polishing, and some small dark Y_2O_3 dendrites remained in the $\sim Y_3(Ru,Ni)$ + Y_2O_3 (originally (Y)) eutectic (Fig. 20). The eutectic structure had two apparent morphologies, with either globular or more needle-like discrete phases, which was an orientation effect. The phases were too small to be analysed individually and accurately. Although there was more of $\sim Y_3(Ru,Ni)$, its analysis was compromised by the (Y) particles in the eutectic structure, thus $\sim Y_3(Ru,Ni)$ should have less Y than was found.

Given the high Y content of the sample, it is likely that (Y) formed first, then oxidized. The solidification reactions were deduced to be:

$$L \rightarrow (Y)\ (\text{which subsequently oxidized})$$

$$L \rightarrow (Y) + \sim Y_3(Ru, Ni).$$

3.2 Heat Treated Samples

Unfortunately, rather than being annealed at 1000 °C as planned, the samples were actually annealed at 1200 °C for 1000 h. This meant that some of the samples experienced partial melting, and there was oxidation in the form of minor rounded oxides in the matrix, while Y loss was often severe. However, the results did give more information on the system.

3.2.1 Nominal Ni_{38}:Ru_{42}:Y_{20} (at.%), Sample 6H. After heat treatment, nominal Ni_{38}:Ru_{42}:Y_{20} (at.%), Sample 6H comprised four different regions of different microstructures, although some were the same phases as in the as-cast sample, which are reported in Table 4 as 6H-1 to 6H-4 from the outside inwards. These four different regions, with two intermediate layers, comprised (Ru) in matrices of $\sim YNi_3$ of two different compositions, $\sim YNi_4$ and $\sim YNi_5$, from the inside to the outside (Fig. 21). The last layer had cracks within $\sim YNi_5$, which usually ran between (Ru) regions. There were very small differences in the (Ru) contents in

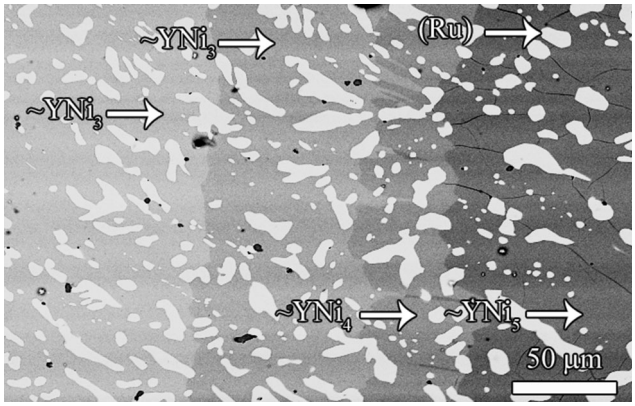

Fig. 21 SEM-BSE image of as-cast nominal Ni_{38}:Ru_{42}:Y_{20} (at.%) (Sample 6H) annealed at 1200 °C for 1000h, showing (Ru) (light) in darker matrices (from left to right): of ~YNi_3 of two different compositions, ~YNi_4 and ~YNi_5, with the centre of the sample being towards the left

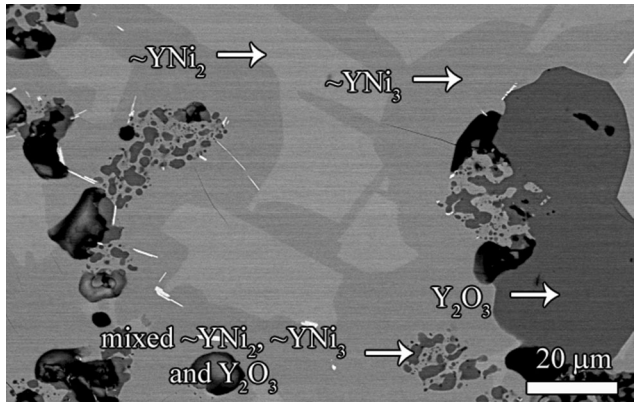

Fig. 22 SEM-BSE image of as-cast nominal Ni_{24}:Ru_{26}:Y_{50} (at.%) (Sample 1H) annealed at 1200 °C for 1000h showing blocks of ~YNi_2 (light) in ~YNi_3 (medium) with Y_2O_3 (dark), and smaller mixed regions of ~YNi_2, ~YNi_3 and Y_2O_3, with some porosity (very dark)

the different regions. Small regions of Y_2O_3 were found throughout the sample, and were rounded and in a much smaller proportions than the Y_2O_3 seen in the as-cast samples.

3.2.2 Nominal Ni_{69}:Ru_{16}:Y_{15} (at.%), Sample 5H. The same phases, (Ru) and ~YNi_5, as in the as-cast sample were found after heat treatment, but they had rounded and coarsened considerably. The sample had lost Ni.

3.2.3 Nominal Ni_{19}:Ru_{46}:Y_{35} (at.%), Sample 3H. The as-cast microstructure of nominal Ni_{19}:Ru_{46}:Y_{35} (at.%), Sample 3, had changed from the ~YRu_2 (inside)/~YNi_2 (outside) dendrites with minor amounts of the univariant binary ~YNi_2 + τ eutectic, to regions of Si on the outside (which were ignored since this was contamination from the ampoules), (Ru) in ~YNi_2; Y_2O_3 in ~YNi_2; and higher proportions of (Ru) variously in adjacent regions of ~YRu_2 and ~YNi_2 (all with minor amounts of rounded oxides).[18] In Table 4, these are denoted as 3H-1 to 3H-4 working inwards in the sample. In 3H-4, a coarsened eutectic-like structure of (Ru) + ~YRu_2 formed, consistent with the Ru-Y binary,[5] at lower temperatures in the ternary.

3.2.4 Nominal Ni_{24}:Ru_{26}:Y_{50} (at.%), Sample 1H. The ~YNi_2 dendrites and τ + ~$Y_{44}Ru_{25}$ univariant binary eutectic microstructure of as-cast Ni_{24}:Ru_{26}:Y_{50} (at.%) (Sample 1 and Fig. 16), had changed totally on heat treatment to blocks of ~YNi_2 in a matrix of ~YNi_3 with large rounded regions of Y_2O_3, and smaller mixed regions of ~YNi_3 and Y_2O_3 (Fig. 22). The latter mixed regions (of composition: 23.4 ± 7.0 Ni, 19.4 ± 1.6 Ru, 57.2 ± 7.6 Y (at.%)) at least had melted, as indicated by the associated coarse porosity, and these regions were taken as the liquid composition. The sample had lost some Y and Ni, and comprised many large pores.

3.2.5 Nominal Ni_{41}:Ru_{16}:Y_{43} (at.%), Sample 4H. As-cast Ni_{41}:Ru_{16}:Y_{43} (at.%) (Sample 4H) comprised τ in ~YNi_2 dendrites in a sparse univariant binary eutectic of ~YNi_2 + ~YNi, whereas after heat treatment, there was severe reaction with the ampoule's silicon and much oxidation. Portions in the centre of the sample, which were surrounded by coarse connected porosity had very similar microstructures to Ni_{24}:Ru_{26}:Y_{50} (at.%) (Sample 1H, Fig. 22), with ~YNi_2, ~YNi_3 and rounded Y_2O_3 (although with no mixed regions). The sample had lost both Y and Ni.

4. Discussion

There were always problems with the (Y) phase being oxidised, despite keeping the samples in alcohol, and methanol was found to be better than ethanol. However, the higher Y content samples were even more problematic. The darkest phases were deduced as oxides because neither ruthenium nor nickel has been reported to have any discernible solubility in Y.[5] Thus, most of the samples had Y_2O_3 and the true presence of (Y) was deduced by the microstructure, the overall composition of the alloy and the solidification sequence. Mostly, the oxide results were ignored in the interpretation of the ternary, although when interpreted as oxidized (Y), they were plotted ignoring the oxygen content (Fig. 23).

Another problem was the contamination of Ta, which was from contamination of the source Y material and was observed more in higher Y content samples. Yttrium was supplied by Goodfellow Metals Cambridge Limited, who stated that the supplied Y lumps could contain up to 300 ppm Ta, as well as other lesser impurities (Table 1) which were not found, being below the EDX detection limit. This problem was exacerbated, because in the energy dispersive x-ray spectra, significant peaks of Ta were overlapped by Ni and Y peaks, and the Ta peaks could only be discerned in the very high Y content alloys. It was deduced that there was no Ta in the matrix (since Y and Ta are nearly exclusively immiscible[5]) and thus the matrix compositions could be used in the phase diagram determination (although Ta is soluble in both (Ni) and (Ru), this higher Y content region is far away

from their solid solutions). This is further substantiated by considering the formation energies: the most negative formation energies were for the intermetallic compounds in the Ni-Y system,[21-23] (YNi_3: −0.402 eV atom^{-1};[24] YNi_2: −0.424 eV atom^{-1};[25] Y_2Ni_7: −0.380 eV atom^{-1};[26] YNi: −0.445 eV atom^{-1}[27]), and although the compounds in the Ni-Ta systems had negative formation energies,[21-23] they were less negative than those of the Ni-Y compounds ($TaNi_3$: −0.366 eV atom^{-1};[28] Ta_2Ni: −0.232 eV atom^{-1};[29] $TaNi_2$: −0.340 eV atom^{-1}[30]). This was also the case for the reported Ru-Ta intermetallic compounds[21-23] (Ta_3Ru: −0.215 eV atom^{-1}; TaRu: −0.317 eV atom^{-1};[31] $TaRu_3$: −0.196 eV atom^{-1}) and the reported ternary compounds[21-23], ($YTaRu_2$: −0.335 eV atom^{-1}; Y_2NiRu: −0.361 eV atom^{-1}).

Yttrium oxidized whereas the Ta did not, because yttrium has an exceptionally high affinity for oxygen, with a free energy of formation of the oxide of 1817 kJ mol^{-1}, probably the highest of any element, and it also dissolves oxygen gas in relatively high concentrations.[32,33] The formation energies of the different structures of Y_2O_3 (−3.846 eV atom^{-1},[21-23,34] −3.809 eV atom^{-1},[21-23,35] −3.784 eV atom^{-1}[21-23,35] and −3.714 eV atom^{-1}[21-23,36]) are all more negative than those of the most stable (i.e. most negative) tantalum oxide (Ta_2O_5 at −3.186 eV atom^{-1}[21-23,37]). Additionally, the amount of oxygen was limited in the closed environment of the arc-melter. When the Ti melted first as the oxygen getter, yttrium would have reacted next with the remaining oxygen (being in the larger proportion than tantalum), and subsequently would have left very little oxygen for Ta oxidation.

The phases were identified by comparing results with the isothermal section at 600 °C,[9] the component binary phase diagrams,[5] and comparing morphologies of the different phases. Limited XRD was undertaken, because by the time the samples had been fully analysed, they had oxidized to such an extent that XRD would have revealed a high proportion of the Y_2O_3 oxide phase. Additionally, at the time of this work, there were insufficient data in the ICDD[38] and Karlsruhe[39] databases for the binary phases, and the patterns of at least some of the phases would have had to be modelled, then compared to the limited data. Even when XRD was undertaken, the spectra were of such a poor quality that they were not helpful.

Some of the deductions are already described in the results of the individual alloys, and these were aided by plotting the compositions on a solidification projection (Fig. 23). For samples with Y_2O_3 which was not considered part of the ternary, the lines between the phases are shown with dotted lines. The solidification temperatures of Samples 1 and 3 must have been fairly different, because the lines between the component phases cross. Although in an isothermal section (i.e. of a specific temperature), the tie-lines are forbidden to cross, since these are as-cast samples, if the solidification ranges are at different temperatures, then the lines between the phases can cross (they are probably not true tie-lines), as long as they lie at a fairly low angle to each other. The lines between the different phases of Samples 1 and 3 are consistent with Sample 3 solidifying at a higher temperature than Sample 1.

The wide solubility range of $\sim YNi_2$ for Ru[7,9] was confirmed, and thus the phase was cored in the as-cast condition. The $\sim Y_3Ni_2$ phase was only found in Sample 10, which would be expected, since it only has a very small liquid surface, and so is unlikely to penetrate very far into the ternary. The same was true for $\sim Y_2Ni_7$. The $\sim Y_3Ru_2$ and $\sim Y_2Ni_{17}$ phases were not found at all. This was partly because of limited penetration into the ternary in both solubility, and liquidus surface. However, not finding $\sim Y_3Ru_2$ could have been due to not having a sample composition near that phase. Not finding $\sim Y_2Ni_7$ is consistent with Sokolovskaya et al.[9-11] Most of the phases had very narrow ranges, except for: $\sim YNi_2$, $\sim YNi_3$ (at least near the Ni-Y system), ∼YNi and $\sim Y_3$(Ru,Ni). The binary phases penetrated into the ternary with constant Y content, agreeing with Sokolovskaya et al.[9-11] and being consistent with their reasoning.[9]

Assuming that the Ta contamination did not affect the other phases in which it did not dissolve, Sample 14 (Ni_{10}:Ru_{12}:Y_{78} (at.%)) indicated that the $\sim Y_3Ru$ and $\sim Y_3Ni$ phases were continuous, at least on solidification, which is possible, since they both have the same *oP*16 structure. However, no samples were made in that region, so this investigation cannot be conclusive on this. A miscibility gap for $\sim Y_3$(Ru,Ni) occurs at lower temperatures, since Sokolovskaya et al.[9-11] found two phases at 600 °C. Sample 14 (Ni_{10}:Ru_{12}:Y_{78} (at.%)) disagrees with Samples 10 and 15, and had more contamination. However, Samples 10 and 15 had the univariant binary $\sim Y_3$(Ru,Ni) + (Y) eutectic. Although the analyses of this eutectic from the different samples were different, due to the small areas analysed and the one degree of freedom of this binary, the true analysis is near the overall composition of Sample 15, since this sample was mostly eutectic. This was taken into account when the liquidus surface (Fig. 24) was drawn.

When compared with the isothermal section at 600 °C of Sokolovskaya et al.[9] the phase widths of line compounds on the YNi_2 to YRu_2 transect of this study were in agreement[9] although wider than the subsequent compiled sections.[10,11] It would be expected that the phase widths at 600 °C would be narrower than on solidification, since solubility tends to decrease with decreasing temperature. The extensions of the binary phase into the ternary were: ∼51 at.% Ru for $\sim YNi_2$; ∼22 at.% Ru for $\sim YNi_3$; ∼13 at.% Ru for $\sim YNi_5$; ∼7 at.% Ru for ∼YNi; and ∼12 at.% Ni for $\sim YRu_2$ and $\sim Y_{44}Ru_{25}$. The ternary $\sim Y_5Ru_2Ni_2$ phase of Sokolovskaya et al.[9-11] was seen in Samples 1, 3, 4, 9, 11, 18 and 19, but at a slightly different composition: $\sim Y_{51}Ru_{15}Ni_{34}$ (at.%), and has been designated τ here (for ternary phase).

The solidification reactions were deduced from the microstructures. The liquidus surface (Fig. 24) was drawn to be consistent with the phases analysed and identified, as well as with the solidification sequences and the accepted binary phase diagrams.[5] The overall compositions of the alloys had to lie on their primary phase liquidus surfaces, but the overall compositions of the univariant binary eutectics were not always accurate, and so did not lie at the junctions of their relevant liquidus surfaces, and those

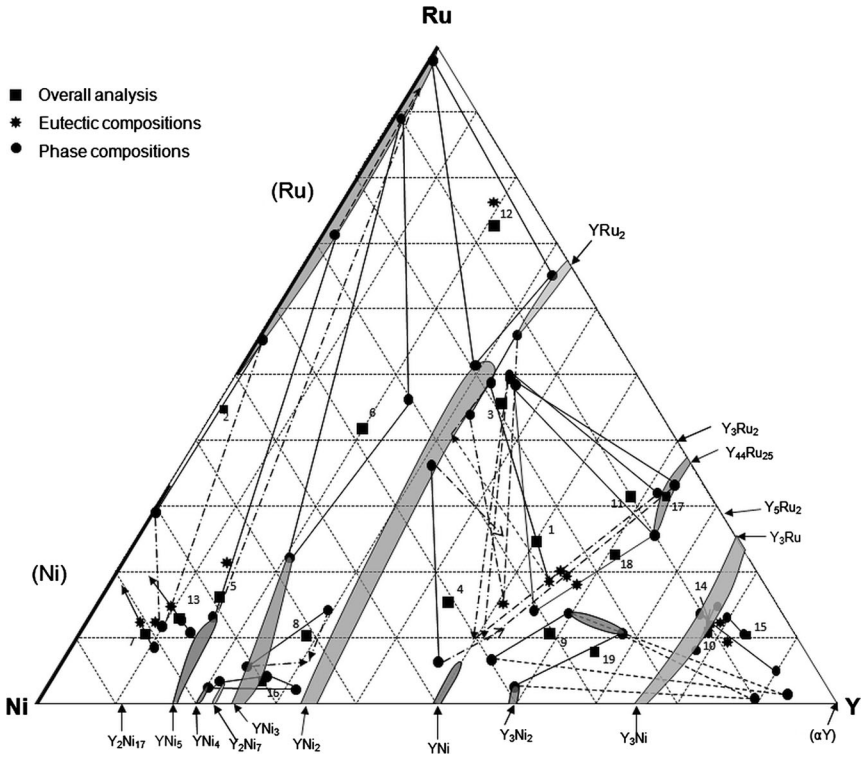

Fig. 23 Solidification projection of the Ni-Ru-Y system (at.%), with phases not present indicated by arrows, and numbers are the sample numbers

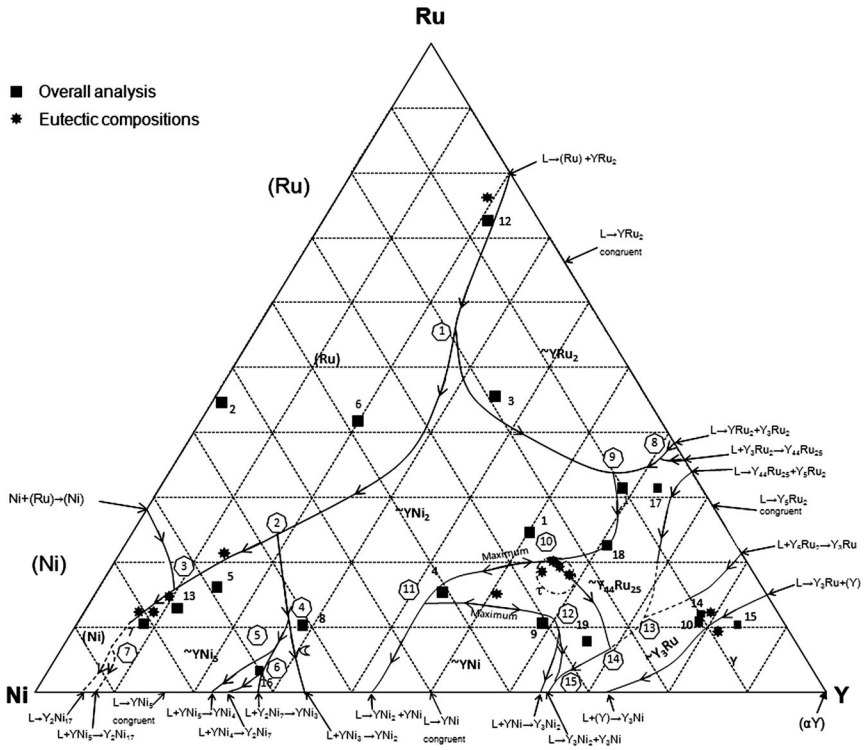

Fig. 24 Liquidus surface projection of the Ni-Ru-Y system (at.%), with phases not present indicated by arrows, numbers are the sample numbers, and enclosed numbers are the reaction numbers

Table 5 Invariant reactions of the Ni-Ru-Y system

Reaction No.	Approximate liquid composition (at.%)	Invariant reaction
1	$Ni_{19}:Ru_{56}:Y_{25}$	$L + (Ru) + \sim YRu_2 \rightarrow \sim YNi_2$
2	$Ni_{58}:Ru_{20}:Y_{22}$	$L + (Ru) + \sim YNi_2 \rightarrow \sim YNi_5$
3	$Ni_{75}:Ru_{15}:Y_{10}$	$L + (Ru) \rightarrow \sim YNi_5 + (Ni)$
4	$Ni_{62}:Ru_{12}:Y_{26}$	$L + \sim YNi_2 + \sim YNi_5 \rightarrow \sim YNi_3$
5	$Ni_{66}:Ru_7:Y_{27}$	$L + \sim YNi_3 + \sim YNi_5 \rightarrow \sim YNi_4$
6	$Ni_{70}:Ru_3:Y_{27}$	$L + \sim YNi_3 + \sim YNi_4 \rightarrow \sim Y_2Ni_7$
7	$Ni_{87}:Ru_7:Y_6$	$L + (Ni) + \sim YNi_5 \rightarrow \sim Y_2Ni_{17}$
8	$Ni_3:Ru_{36}:Y_{61}$	$L + \sim Y_3Ru_2 \rightarrow \sim YRu_2 + \sim Y_{44}Ru_{25}$
9	$Ni_{10}:Ru_{34}:Y_{56}$	$L + \sim YRu_2 \rightarrow \sim YNi_2 + \sim Y_{44}Ru_{25}$
10	$Ni_{25}:Ru_{21}:Y_{54}$	$L + \sim YNi_2 \rightarrow \sim Y_{44}Ru_{25} + \tau$
Maximum	$Ni_{33}:Ru_{18}:Y_{49}$	$L + \sim YNi_2 \rightarrow \tau$
11	$Ni_{44}:Ru_{14}:Y_{42}$	$L + \tau \rightarrow \sim YNi_2 + \sim YNi$
Maximum	$Ni_{36}:Ru_{14}:Y_{50}$	$L + \tau \rightarrow \sim YNi$
12	$Ni_{28}:Ru_{12}:Y_{60}$	$L + \sim YNi + \tau \rightarrow \sim Y_3Ni_2$
13	$Ni_{17}:Ru_{12}:Y_{71}$	$L + \sim Y_5Ru_2 \rightarrow \sim Y_{44}Ru_{25} + \sim Y_3(Ru,Ni)$
14	$Ni_{24}:Ru_7:Y_{69}$	$L + \sim Y_{44}Ru_{25} \rightarrow \tau + \sim Y_3(Ru,Ni)$
15	$Ni_{32}:Ru_3:Y_{65}$	$L + \tau \rightarrow \sim Y_3Ni_2 + \sim Y_3(Ru,Ni)$

known to be inaccurate (due to their small areas) were only used as guidelines (Samples 1, 2, 3, 10 and 12). Although the univariant nature of these binary eutectic reactions would allow for changing overall compositions, this should not have moved the analysed compositions from the surface junctions, and so it is likely that the small eutectic regions were causing the inaccuracies. In order for Sample 8 to solidify as interpreted, with $\sim YNi_2$ forming before $\sim YNi_3$, the addition of Ru raises the liquidus temperature for primary $\sim YNi_2$ relative to that of primary YNi_3. This is consistent with $\sim YNi_2$ being stabilized by Ru, and so solidifying at higher temperatures than in the Ni-Y system. The directions of the reactions were drawn so that the reactions observed could be produced. For example, the microstructure of Sample 11 necessitated the $L + \sim YNi_2 \rightarrow \sim Y_3Ru_2 + \tau$, $\sim Y_{51}Ru_{15}Ni_{34}$ invariant reaction, and so the arrows were drawn accordingly. The coarsening of the $\sim YNi_2 + \sim Y_{44}Ru_{25}$ eutectic structure by the large growth of $\sim YNi_2$ in the solid state means that the $\sim Y_{44}Ru_{25}$ solvus retreats significantly at decreasing temperatures, which agrees with Sokolovskaya et al.[9-11] not reporting it at 600 °C below ~5 at.% Ni.

None of the samples had the Y_5Ru_2 phase, and even though it forms congruently, it only has a small liquidus surface in the binary,[5] so lacking any other indication, it has been given a relatively small liquidus surface in the ternary. This and $\sim Y_2Ni_{17}$ were the only liquidus surfaces for which there was no indication from the current samples, and so they are shown by dotted lines in Fig. 24. The solidification reactions were either directly observed in the samples, or derived from the liquidus surface, and are shown in Table 5. In order to experience the reactions observed in the microstructures, the univariant equilibria $L \rightarrow \tau + \sim YNi_2$ and $L \rightarrow \tau + YNi$ must each have a maximum, which is consistent with the congruent solidification of YNi in the binary.[5]

On heat treatment, despite precautions, the samples lost Y ($Ni_{38}:Ru_{42}:Y_{20}$ (at.%) to Sample 6H), or Ni ($Ni_{69}:Ru_{16}:Y_{15}$ (at.%) to Sample 5H), or both ($Ni_{24}:Ru_{26}:Y_{50}$ (at.%) to Sample 1; $Ni_{19}:Ru_{46}:Y_{35}$ (at.%) to Sample 3H). The $Ni_{38}:Ru_{42}:Y_{20}$ (at.%) alloy (Sample 6H) showed that the Y was lost on heat treatment, since the layers became less Y-rich towards the outside. There was also evidence that the $\sim YNi_4$ layer formed by diffusion at the $\sim YNi_3/\sim YNi_5$ interface, since there were still small regions where this interface still existed (Fig. 20).

When the isothermal section at 1200 °C was plotted (Fig. 25), there was mainly (Ru), $\sim YRu_2$, $\sim YNi_2$, $\sim YNi_3$, $\sim YNi_4$, $\sim YNi_5$ and (Y) (Y_2O_3). The other phases were missing because of their lower melting points (e.g. $\sim YNi_2$, $\sim YNi$, $\sim Y_3Ni_2$ and $\sim Y_3Ni$), small penetration into the ternary (e.g. $\sim Y_2Ni_{17}$ and $\sim Y_2Ni_7$), lack of an annealed sample near the phase compositions (e.g. (Ni), or both the last two reasons (e.g. $\sim Y_3Ru_2$, $\sim Y_{44}Ru_{25}$, $\sim Y_5Ru_2$ and $\sim Y_3Ru$). The mixed phase regions of Sample 1H were taken as the liquid composition at 1200 °C. The $\sim YNi_3$ phase had a larger extension than at 600 °C,[9] which is consistent with solubility decreasing with temperature. The increased stability of $\sim YNi_2$ agrees with the liquidus surface. The τ phase ($\sim Y_{51}Ru_{15}Ni_{34}$) was not found at 1200 °C, indicating that it solidifies below 1200 °C.

5. Conclusions

Despite problems with oxidation of Y and its contamination by Ta, consistent interpretations were made using EDX results and phase morphologies. A solidification projection and a liquidus surface projection were drawn and were in agreement with the binary systems and the 600 °C isothermal section of Sokolovskaya et al. The $\sim YRu_2$, $\sim YNi_2$ and

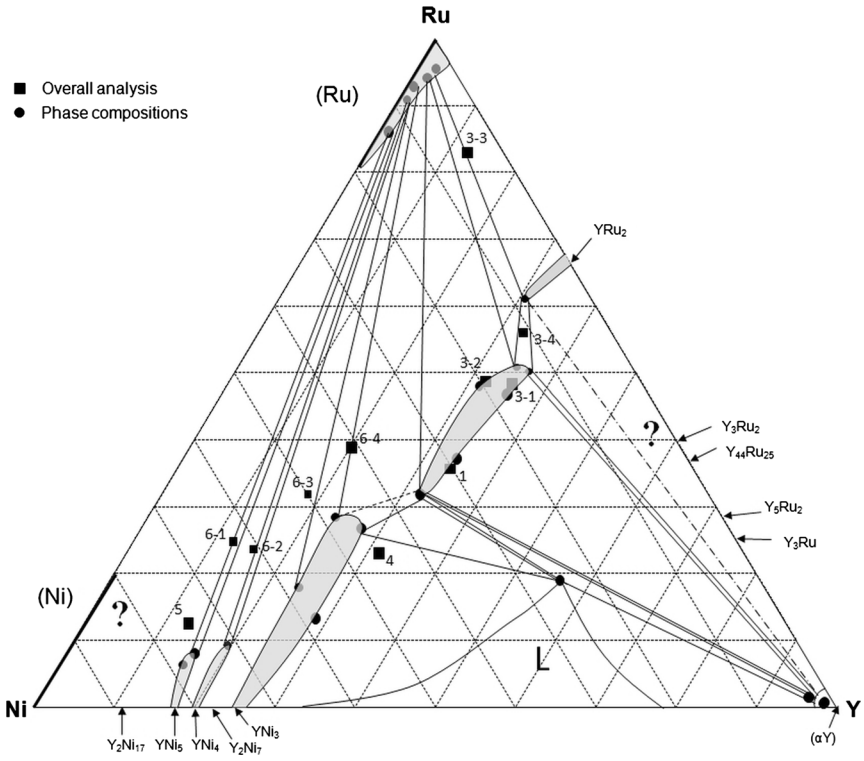

Fig. 25 Isothermal section at 1200 °C of the Ni-Ru-Y system (at.%), with phases not present indicated by arrows, and numbers are the sample numbers

$\sim YNi_3$ phases have wider solubilities than at 600 °C, which is expected. The binary phase extensions into the ternary were: ~51 at.% Ru for $\sim YNi_2$; ~22 at.% Ru for $\sim YNi_3$; ~13 at.% Ru for $\sim YNi_5$; ~7 at.% Ru for ~YNi; and ~12 at.% Ni for $\sim YRu_2$ and ~10 at.% Ni for $\sim Y_{44}Ru_{25}$. On solidification, the $\sim Y_3$(Ru,Ni) phase was seen, which indicates a miscibility gap above 600 °C, to give $\sim Y_3Ru$ and $\sim Y_3Ni$ as separate phases, as observed by Sokolovskaya et al. Only the $\sim Y_3Ru_2$ and $\sim Y_2Ni_{17}$ phases were not found, due to limited penetration into the ternary, and $\sim Y_3Ni_2$ and $\sim Y_2Ni_7$ were also seen to have very limited extents. One ternary phase was found at $\sim Y_{51}Ru_{15}Ni_{34}$ (at.%), which is a slightly different composition than reported before. Heat treatment at 1200 °C gave the phases: (Ru), $\sim YRu_2$, $\sim YNi_2$, $\sim YNi_3$, $\sim YNi_4$, $\sim YNi_5$ and (Y). The higher formation temperature of $\sim YNi_2$ in the ternary was seen in both the liquidus projection and the isothermal section at 1200 °C and is due to the stabilization by Ru.

Acknowledgments

The assistance of the Department of Science and Technology and the National Research Foundation (South Africa), Carnegie-IAS, Mintek and the University of Botswana ORD are gratefully acknowledged.

References

1. J.H. Potgieter, A. van Bennekom, and P. Ellis, Investigation of the Active Dissolution Behaviour of a 22% Chromium Duplex Stainless Steel with Small Ruthenium Additions in Sulphuric Acid, *ISIJ Int.*, 1995, **35**(2), p 197-202
2. T.L. Shing, S. Luyckx, and I.T. Northrop, The Effect of Ruthenium Additions on the Hardness, Toughness and Grain Size of WC-Co, *Int. J. Refract. Met. Hard Mater.*, 2001, **19**(1), p 41-44
3. E. van der Lingen and R.F. Sandenbergh, Cathodic Modification Behaviour of Ruthenium Additions to Titanium in Hydrochloric Acid, *Corr. Sci.*, 2001, **43**(3), p 577-590
4. S. Grainger, Ed., *Engineering Coatings—Design and Application*, Abington Publishing, Cambridge, 1989
5. T.B. Massalski, H. Okamoto, P.R. Subramanaian, and L. Kacprzak, *Binary Alloy Phase Diagrams*, 2nd ed., ASTM International, Materials Park, 1990, vol. 3, Ni-Ru p 2850-2851; Ni-Y p 2884-2885; Ru-Y p 3269, 3271; O-Y p 2936-2937; Ru-Ta p 3255-3258; Ni-Ta p 2865, 2867-2868
6. E.F. Tolkunowa, V.V. Burnashova, M.B. Raevskaya, and E.M. Sokolovskaya, Laves Phases Interaction in Y-Ru-Fe Co, Ni Alloy Systems, *Metallofizika*, 1974, **52**, p 109-111
7. H. Chunxiao, M. Guangchen, W. Wenna, W. Yongli, and Z. Huaizhi, *Phase Diagrams of Precious Metal Alloys*, The Metallurgical Industry Press, Beijing, 1983, p 275
8. W.B. Pearson, *A Handbook of Lattice Spacings and Structures of Metals and Alloys*, Pergamon Press, New York, vol. 1, (1958)
9. E.M. Sokolovskaya, M.V. Raevskaya, and E.F. Kazakova, The Influence of Ruthenium on the Stability of Intermetallic Compounds of the Rare-earth Metals, *Moscow Univ. Chem.*

Bull. 1985, **40**, p 71-76 (*Engl. Transl.*), *from Vestnik Moskovskogo Universiteta, Khimiya,* 1985, **26**(3), p 295-301
10. P. Villars, A. Prince, and H. Okomoto, *Handbook of Ternary Alloy Phase Diagrams*, Vol 10, ASM International, Materials Park, 1995, p 12993-12995
11. P. Villars, H. Okomoto, and K. Cenzual, Eds., ASM Alloy Phase Diagrams Center, http://www.asminternational.org/AsmEnterprise/APD, ASM International, Materials Park, 2007, **10**, p 12993, 12995-12996
12. D.G. Pettifor, The Structures of Binary Compounds. I. Phenomenological Structure Maps, *J. Phys. C*, 1986, **19**, p 285-313
13. S.H. Coetzee, L.A. Cornish, and M.J. Witcomb, Solidification of Selected As-Cast Ni-Ru-Y Samples, *Microsc. Microanal.*, 2005, **11**(Suppl 2), p 1844-1845
14. S.H. Coetzee, L.A. Cornish, M.J. Witcomb, and P.K. Jain, Comparison of As-cast Results of Ni-Ru-Y with a 600 °C Isothermal Section, *Proc. 44th Ann. Conf. Microsc. Soc. South. Afr.*, T.A.S. Aveling, K. Marcus, B.T Sewell, J. Theron, and J. Wesley-Smith, Eds., Dec 5-7 (Pietermaritzburg), MSSA, 2005, p 10
15. S.H. Coetzee, L.A. Cornish, and M.J. Witcomb, Derivation of the Liquidus Surface of the Ni-Ru-Y System using SEM and EDX, *Microsc. Microanal.*, 2007, **13**(Suppl 2), p 1052-1053
16. S.H. Coetzee, L.A. Cornish, and M.J. Witcomb, A Study of the Ni-Ru-Y System at 1200 °C Using SEM and EDX, *Microsc. Microanal.*, 2008, **14**(Suppl 2), p 578-579
17. L.A. Cornish, M.J. Witcomb, S.H. Coetzee, W. Tshawe, and S. Prins, *Anomalies and Pitfalls in Phase Analyses Using BSE*, Proc. 46th Ann. Conf. Microsc. Soc. South. Afr., T.A.S. Aveling, R. Knutsen, B.T Sewell, J. Theron, and J. Wesley-Smith, Eds., July 23-35 (Gaborone), MSSA, 2008, p 9
18. S.H. Coetzee, *The Constitution of the Ni-Ru-Y Ternary System*, M.Phil. Dissertation, University of Botswana, 2008
19. S.H. Coetzee, L.A. Cornish, M.J. Witcomb, and P.K. Jain, Progress on the Liquidus Surface Diagram for the Ni-Ru-Y System, *Proc. 47th Ann. Conf. Microsc. Soc. South. Afr.*, T.A.S. Aveling, R. Knutsen, B.T. Sewell, Eds., Dec 8-11 (Durban) MSSA, 2009, p 78
20. J. Emsley, *Nature's Building Blocks: An A-Z Guide to the Elements*, Oxford University Press, 2011, p 495
21. S. Curtarolo, W. Setyawan, S. Wang, J. Xue, K. Yang, R.H. Taylor, L.J. Nelson, G.L.W. Hart, S. Sanvito, M. Buongiorno-Nardelli, N. Mingo, and O. Levy, AFLOWLIB.ORG: A Distributed Materials Properties Repository from High-Throughput AB Initio Calculations, *Comput. Mater. Sci.*, 2012, **58**, p 227-235
22. S. Curtarolo, W. Setyawan, G.L.W. Hart, M. Jahnatek, R.V. Chepulskii, R.H. Taylor, S. Wang, J. Xue, K. Yang, O. Levy, M. Mehl, H.T. Stokes, D.O. Demchenko, and D. Morgan, AFLOW: An Automatic Framework for High-Throughput Materials Discovery, *Comput. Mater. Sci.*, 2012, **58**, p 218-226
23. J.E. Saal, S. Kirklin, M. Aykol, B. Meredig, and C. Wolverton, Materials Design and Discovery with High-Throughput Density Functional Theory: The Open Quantum Materials Database (OQMD), *JOM*, 2013, **65**, p 1501-1509
24. B.J. Beaudry and A.H. Daane, Yttrium-nickel System, *Trans. Am. Inst. Min. Metall. Pet. Eng.*, 1960, **218**, p 854-859
25. J.F. Smith and D.A. Hansen, The structures of YNi_3, YCo_3, $ThFe_3$ and $GdFe_3$, *Acta Crystallogr.*, 1965, **19**, p 1019-1024
26. A. Raman and A.V. Virkar, Crystal structures of AB_3 and A_2B_7 rare earth—nickel phases, *J. Less-Common Met.*, 1969, **18**(1), p 59-66
27. K.O. Klepp and E. Parthé, Yttrium-Nickel YNi with the FeB Structure Type, *Acta Crystallogr. Sect. B*, 1980, **36**, p 3093-3094
28. H. Nowotny and H. Oesterreicher, Die Kristallstrukturen von β-TaNi3, Ta(Cu, Al)2, Nb(Cu, Al)2 und Ta6(Cu, Al)7, *Mh. Chem.*, 1964, **95**(3), p 982-989
29. P.I. Kripyakevich, and E.N. Pylaeva, Crystal Structure of the Compound Ta_2Ni, *Zhurnal Strukturnoi Khimii (J. Struct. Chem.)*, 1962, **3**(1), p 30-32
30. P.I. Kripyakevich and E.N. Pylaeva, Crystalline Structure of Some Compounds in the Nb-Ni and Ta-Ni Systems, *Kristallografiya*, 1967, **12**, p 350-352
31. T. Tsukamoto, K. Koyama, A. Oota, and S. Noguchi, Study of Structural Transformation in Near-Equiatomic M-Ru (M=V, Nb, Ta) Alloys Based on the Electron Theory, *Nippon Kinzoku Gakkai-si*, 1989, **53**(3), p 253-257
32. Lanthanide Lanthology, Part II, Molycorp Inc. Mountain Pass, California, 1994, p 54
33. T.H. Okabe, T.N. Deura, T. Oishi, K. Ono, and D.R. Sadoway, Electrochemical Deoxidation of Yttrium-Oxygen Solid Solutions, *J. Alloys Compd.*, 1996, **237**(1-2), p 150-154
34. M. Faucher and J. Pannetier, Refinement of the Y_2O_3 Structure at 77 K, *Acta Crystallogr. Sect. B*, 1980, **36**(12), p 3209-3211
35. B. Wu, M. Zinkevich, F. Aldinger, D. Wen, and L. Chen, Ab Initio Study on Structure and Phase Transition of A- and B-Type Rare-Earth Sesquioxides Ln_2O_3 (Ln= La-Lu, Y and Sc) Based on Density Function Theory, *J. Solid State Chem.*, 2007, **180**(11), p 3280-3287
36. R.M. Wentzcovitch and K. Umemoto, Effect of the d Electrons on Phase Transitions in Transition-Metal Sesquioxides, *Phys. Chem. Miner.*, 2011, **38**(5), p 387-395
37. P.E. Werner, I.P. Zibrov, M. Sundberg, and V.F. Filonenko, Structures and Phase Transitions of B-Ta_2O_5 and Z-Ta_2O_5: Two High-Pressure Forms of Ta_2O_5, *Acta Crystallogr. Sect. B*, 2000, **56**, p 659-665
38. International Centre for Diffraction Data (ICDD), *Powder Diffraction File (PDF-2)*, 12 Campus Boulevard, Newton Square, 2005
39. http://www.fiz-karlsruhe.de/icsd